Postglacial flooding and Holocene climate shifts in the Persian Gulf

Abdolmajid Naderi Beni, Guillaume Leduc, Morteza Djamali, Arash Sharifi, Nick Marriner, Kazuyo Tachikawa, Frauke Rostek, Mahboubeh Molavi Arabshahi, Rik Tjallingii, Hamid Lahijani, et al.

To cite this version:

Abdolmajid Naderi Beni, Guillaume Leduc, Morteza Djamali, Arash Sharifi, Nick Marriner, et al.. Postglacial flooding and Holocene climate shifts in the Persian Gulf. Journal of Quaternary Science, 2024, 39 (4), pp.592-607. ⟨10.1002/jqs.3614⟩. ⟨hal-04508491⟩

HAL Id: hal-04508491
https://hal.science/hal-04508491v1

Submitted on 13 Nov 2024

Postglacial flooding and Holocene climate shifts in the Persian Gulf

ABDOLMAJID NADERI BENI,[1]* GUILLAUME LEDUC,[2] MORTEZA DJAMALI,[3] ARASH SHARIFI,[4,5] NICK MARRINER,[6] KAZUYO TACHIKAWA,[2] FRAUKE ROSTEK,[2] RIK TJALLINGII,[7] HAMID LAHIJANI,[1] MAHBOUBEH MOLAVI ARABSHAHI,[8] MARTA GARCIA,[2] LAETITIA LICARI,[2] MARTIN TETARD,[2,9] MARIE-CHARLOTTE BELLINGHERY[3] and EDOUARD BARD[2]
[1]Iranian National Institute for Oceanography and Atmospheric Science, Tehran, Iran
[2]CEREGE, Aix Marseille University, CNRS, IRD, INRAE, Collège de France, Aix-en-Provence, France
[3]Institut Mediterraneen de Biodiversite et d'Ecologie Marine et Continentale (IMBE), IMBE – UMR Aix Marseille Universit e, CNRS, IRD, Avignon Universite, France
[4]Neptune Isotope Laboratory (NIL), Department of Marine Geosciences, Rosenstiel School of Marine and Atmospheric Science, Key Biscayne, FL, USA
[5]BETA Analytic-Isobar Science, Research and Development Department, Miami, FL, USA
[6]CNRS, TheMA UMR 6049, Universite de Bourgogne Franche-Comte, Besançon, France
[7]GFZ German Research Centre for Geosciences, Section 4.3 Climate Dynamics and Landscape Evolution, Potsdam, Germany
[8]School of Mathematics, Iran University of Science and Technology, Tehran, Iran
[9]GNS Science, Lower Hutt, New Zealand

Received 5 October 2023; Revised 18 February 2024; Accepted 23 February 2024

ABSTRACT: Postglacial flooding of the Persian Gulf (PG) was important in shaping human history and driving landscape changes in the region. However, there is a paucity of data regarding the postglacial transgression. The position of the PG at the edge of major synoptic systems of the Indian Ocean Summer Monsoon (IOSM) and Mid-latitude Westerlies (MLW) makes the environment particularly sensitive to Holocene climate shifts. To investigate the timing of the flooding and to detect the impacts of significant climate shifts on the regional environment during the Holocene, a multiproxy study was conducted on three short sediment cores from two deep sites in the PG. Sedimentological, palynological and geochemical analyses were performed on the cores. The results show that inundation of the western part of the PG that started from ca. 11.5 ka BP continued with successive prominent phases of transgression centered on 10.4 and 9.2 ka cal BP, and definitive marine conditions were established around 8.8 ka cal BP. The IOSM was the dominant system in the region until about 9 to ~6.3 ka cal BP. After that time, the intensity of the IOSM declined, as MLW dominated the region after ~6.3 ka cal BP. These climatic shifts induced significant changes in regional vegetation and hydrology, and possibly triggered socio-cultural transformations.

KEYWORDS: Indian Ocean Monsoon; marine transgression; Mid-latitude Westerlies; Persian Gulf

Introduction

Global sea-level reached its lowest point during the Last Glacial Maximum (ca. 20 ka BP) (Mix et al., 2001). This led to the exposure of many continental shelf areas, including the epicontinental basin of the Persian Gulf (PG), which emerged as an alluvial plain in the northwestern corner of the Indian Ocean (Uchupi et al., 1999). Postglacial flooding then inundated the PG in successive phases (Lambeck, 1996), and a new semi-enclosed basin was formed at the heart of the desert belt, where today a subtropical arid to hyper-arid climate is dominant (Djamali et al., 2011). Along with this transgression, Holocene hydroclimatic variations also profoundly affected the regional climate which is mainly governed by the interplay between the Indian Ocean Summer Monsoon (IOSM) and the Mid-latitude Westerlies (MLW) (Gupta et al., 2003).

The geographical position of the PG at the edge of the IOSM and the MLW made it susceptible to transient climatic shifts during the Holocene (Sirocko et al., 1993). The early Holocene climate of the region is marked by an intensification of the IOSM (Fleitmann et al., 2007), followed by a major shift in climatic conditions around 6300 years ago when the MLW was re-established over West Asia (Bar-Matthews and Ayalon, 2011; Sharifi et al., 2015). Holocene meridional migrations of the Inter-Tropical Convergence Zone (ITCZ) (Fleitmann et al., 2003) and the MLW jet (Sharifi et al., 2018), along with the interaction between the MLW and IOSM (Gupta et al., 2003), serve as key controlling mechanisms for the region's climate. These factors have significantly influenced human–environment interactions in western Asia over time (e.g. Djamali et al., 2010; Sharifi et al., 2015).

According to Lambeck (1996), human development in West Asia has been closely linked with evolution of the PG. From the Late Pleistocene to early Holocene, the exposed basin of the PG was a particularly conducive environment to human settlement (Kennett and Kennett, 2007). The availability of water through the river systems and freshwater springs, and favorable temperatures, made the PG basin a key environment for human development (Lambeck, 1996). During the mid-Holocene, the water level of the PG reached its zenith, aligning with global sea level (Lambeck, 1996). The PG reached around 1–2 m above the current level and submerged low-lying coastal areas (Heyvaert and Baeteman, 2007). Formation of the PG during the Late Pleistocene to early Holocene would have forced early human settlers of PG basin to migrate to surrounding lands (Kennett and Kennett, 2007).

Today, ongoing climatic change is triggering significant environmental changes in the region with socio-economic consequences (Naderi Beni et al., 2021). Studies indicate a northward propagation of the ITCZ and intensified IOSM since 2002 (Hari et al., 2020), mirroring conditions observed during the early Holocene. Compounding these changes is the rising sea level

---

*Correspondence: Abdolmajid Naderi Beni, as above.
E-mail: amnaderi@inio.ac.ir

of the PG at rates exceeding 3.5 mm a^{-1} (Naderi Beni et al., 2021). Acknowledging the importance of assessing long-term perspectives (Bradley, 2000), paleoenvironmental studies play a crucial role in understanding climatically induced environmental shifts and their consequences.

Despite the importance of postglacial flooding of the PG and the regional Holocene climatic changes in shaping the landscape and human history, numerous knowledge gaps remain regarding the timing of this postglacial flooding and its regional environmental impacts. Only a few studies have been conducted on late Quaternary sediments of the PG (e.g. Purser, 2012; Uchupi et al., 1999). These studies were based on short sediment cores, often lacking robust chronologies that prevent high-resolution multiproxy analysis. Lack of robust sedimentological evidence hinders the validation of geophysical models, hampering estimates of postglacial sea-level rise (Lambeck, 1996).

Given the semi-enclosed nature of the basin, the PG experiences substantial influences from its surrounding lands (Purser, 2012). Local winds transport aeolian sediments mainly from the south and west, freshwater inputs originate from the north and northwest, and fluvial sediments originate from mountains to the north. This combination makes the PG a repository for preserving the impacts of paleoenvironmental changes on the adjacent lands, coupled with the basin's transition from an alluvial to a marine environment.

The extensive catchment basins of the PG, spanning from the subtropical low latitudes in the IOSM regions to higher latitudes in the MLW domain, led us to hypothesize that the sedimentary deposits of the PG reflect not only postglacial flooding but also the interplay between the MLW and IOSM and subsequent environmental changes during the Holocene (Djamali et al., 2010; Gupta et al., 2003; Sharifi et al., 2018). To test this hypothesis, we examined three sediment cores from two sites situated in the deepest parts of the PG to: (i) investigate the timing of postglacial flooding; and (ii) investigate climate shifts in the region during the Holocene and their environmental consequences.

We adopted a multi-proxy methodology, incorporating sedimentological, palynological, and organic and inorganic geochemical analyses. This comprehensive methodology allowed us to identify the period of flooding using high-resolution assessments. Additionally, low-resolution analyses have shed light on environmentally induced changes, such as shifts in vegetation types during the early Holocene. These insights contribute to the overall robustness of our findings.

Study area

The PG is a semi-enclosed epicontinental basin with an average depth of 35 m. This meso-tidal water body is connected to the Arabian Sea through the narrow Strait of Hormuz (Fig. 1), where the maximum depth of the basin is recorded at ~110 m (Kämpf and Sadrinasab, 2006). The basin formed as a result of the northward movement and collision of the Arabian Shield in relation to the Eurasian lithospheric plate (Iranian continental block) (Konyuhov and Maleki, 2006). The collision zone is marked by the NW–SE Zagros mountain range, whereas the PG and Mesopotamian basins were formed as foreland basins (Konyuhov and Maleki, 2006) (Fig. 1).

The PG is divided into a northern part with a steeper slope, hosting the deepest and tectonically unstable areas (Konyuhov and Maleki, 2006), and a southern section within the tectonically stable Arabian Shield, featuring shallow waters (Purser, 2012). The basin's epicontinental nature and complex geological setting result in intricate bottom topography, creating diverse sub-environments.

Geomorphologically, four main sub-basins can be identified in the PG (Fig. 1); the Mesopotamian Shallow Shelf (MSS) lies at the head of the PG, where the Mesopotamian river system discharges into the basin. The river system is the most important freshwater source that drains the southern flanks of the Taurus–Zagros mountains through the Mesopotamian basin into the PG, and its delta extends around 100 km eastward into the basin (Fig. 1). On average, the river discharges >45 km^3 a^{-1} and total sediment runoff of 105 million tons per year since the 1930s, but this has decreased to 53 million tons per year in recent years due to the impacts of dam construction and climate change (Naderi Beni et al., 2021; Isaev and Mikhailova, 2009). The MSS gently merges in to the Western Sub-Basin (WSB), where water depth reaches >60 m (Purser, 2012). The Eastern Sub-Basin (ESB), with a depth of >80 m, is isolated from the WSB by a sill, and from the Strait of Hormuz by another sill to the east (Purser, 2012). Most of the southern part of the PG belongs to the Arabian Shallow Shelf (ASH), which is characterized by a very gentle slope, relatively high degree of wave agitation and high temperature that lead to classic carbonate precipitation (Purser, 2012).

The climate of the PG is primarily governed by the MLW, with additional influence from the IOSM in the east (Thoppil and Hogan, 2010). Absolute summer sea-surface temperature exceeds 35 °C, dropping to <10 °C in winter. The northerly Shamal wind, a notable regional climatic feature, causes strong stratification in deep PG waters during summer (Saleh et al., 2021). In winter, the Shamal wind and low temperatures induce convective vertical mixing, eradicating summer stratification, and strengthening circulation, leading to strong coastal currents (Thoppil and Hogan, 2010). High evaporation and Shamal winds contribute to elevated water salinity, exceeding 39 practical salinity unit (PSU) in the open sea and 100 PSU in the ASH coastal waters and lagoons (Kämpf and Sadrinasab, 2006). Less saline water from the Indian Ocean compensates for evaporated water, entering mainly as surface water from the northern Strait of Hormuz. Simultaneously, warm and salty water from the PG is discharged into the Arabian Sea through the southern Strait's bottom layer (Kämpf and Sadrinasab, 2006).

Seasonal variations in the PG result in varying dense water formation. Winter sees dense water in the northern and southwestern parts, while summer witnesses warmer and hypersaline waters in the southwestern part. Dense water constantly advects from the northern coast towards the Strait of Hormuz, and saline water exits from the southwestern evaporative area occur in late summer and autumn (Pous et al., 2015). Winds, tidal currents and density-driven circulation significantly shape water motion (Kämpf and Sadrinasab, 2006). As a corollary, circulation in the PG, and consequently sediment transportation, exhibits a complexity beyond a simple anticlockwise pattern. This complexity is shaped by seasonal variations, discharge rate of the Mesopotamian river system, wind forcing, tides and intricate bottom topography (Pous et al., 2015).

Rivers originating from the Zagros Mountains, along with the Mesopotamian river system, are key contributors to clastic sediments (Al-Yamani, 2008). Additionally, the Shamal wind transports ~100 million tons of sediment annually eastward (Pye, 1987). Aeolian deposits significantly influence sedimentation rates in both the MSS and WSB (Al-Yamani, 2008). Furthermore, biogeochemical carbonate precipitation plays a crucial role in sediment composition, particularly in the ASH (Purser, 2012).

Materials and methods

Two sediment cores from the WSB (PG-51 and PG-51S) and one sediment core from the ESB (PG-104) were retrieved in

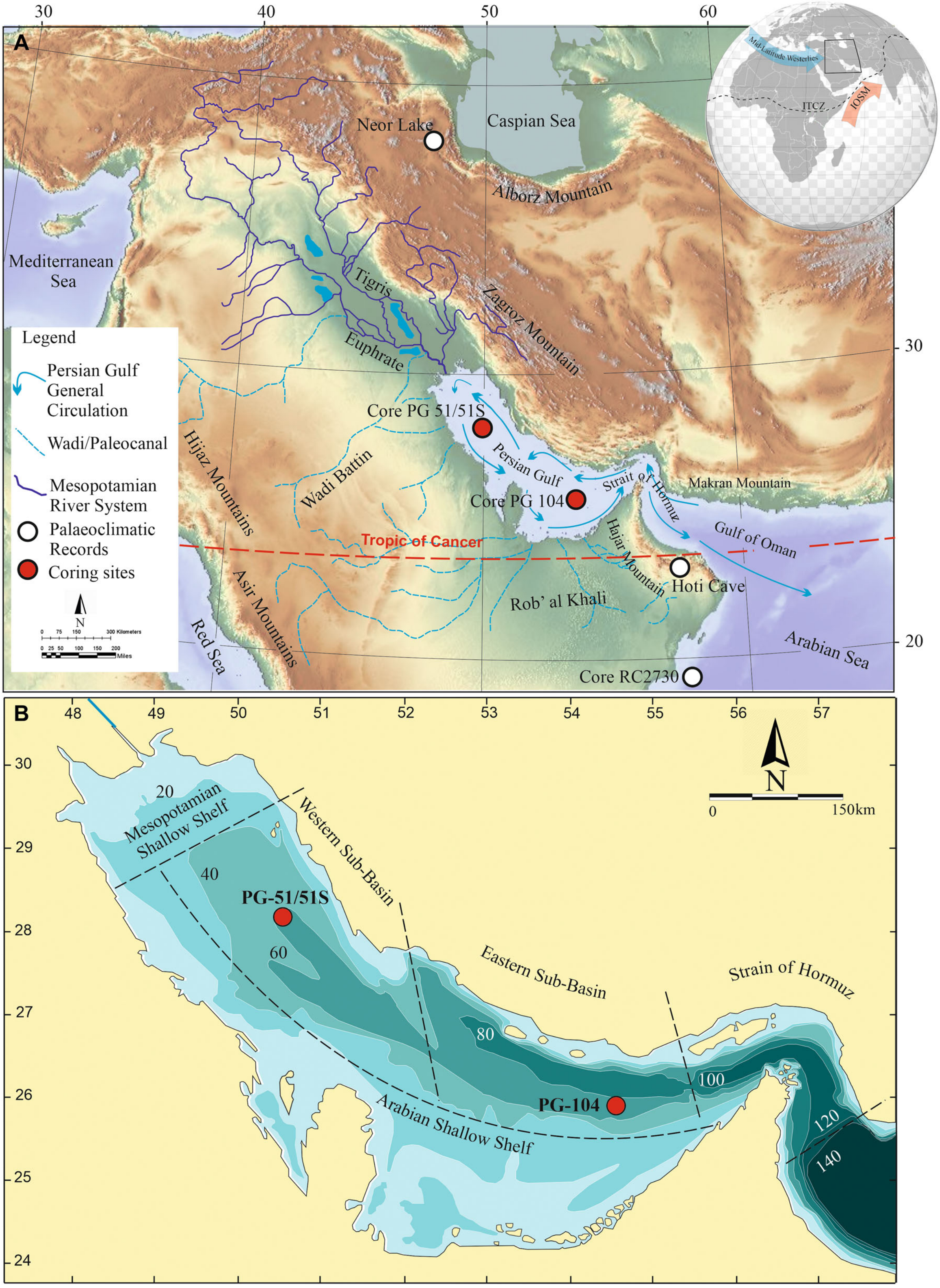

Figure 1. General map of the study area. (A) The position of the Persian Gulf in the northwestern Indian Ocean, the regional topography and main river systems discharging into the Persian Gulf. The general water circulation pattern in the Gulf (Kämpf and Sadrinasab, 2006) is shown by blue arrows. Red circles denote the position of coring sites, and white circles show other mentioned regional archives: Neor Lake (Sharifi et al., 2015), Hoti Cave (Fleitmann et al., 2003) and Core RC2730 (Gupta et al., 2003). The position of the ITCZ and major climatic systems in the study area (MLW and IOSM) are presented in the inset globe on the upper right corner of the map. (B) Bathymetry of the Persian Gulf and its main geomorphological domains. Red circles denote the position of sampling sites. [Color figure can be viewed at wileyonlinelibrary.com]

2012 using a gravity corer. The PG-51 and PG-51S cores were analyzed for magnetic susceptibility (MS) through the coil of a Bartington MS2C system at 2-cm resolution. After splitting, half of the PG-51 core was subsampled for sedimentological analysis at the Iranian National Institute for Oceanography and Atmospheric Science (INIOAS) laboratory. The remaining subsamples of core PG-51 and the intact cores PG-51S and PG-104 were then shipped to France and opened at CEREGE Laboratory for further sedimentological, palynological and geochemical measurements (Table 1).

Table 1. Location of the three studied cores and analysis performed on each of them.

Sediment core characteristics					Laboratory analysis						
Core ID	Position	Length (cm)	Water depth (m)	SED	XRF	^{14}C	OG	C/N	PAL	MS
PG-51S	28.24°N, 50.54°E	83	60	✓	✓	–	–	–	–	✓
PG-51	28.24°N, 50.54°E	129	60	✓	–	✓	✓	–	✓	✓
PG-104	25.68°N, 54.42°E	122	78	✓	✓	✓	–	✓	–	–

^{14}C, radiocarbon age dating; C/N, carbon to Nitrogen ratio; MS, magnetic susceptibility; OG, organic geochemistry; PAL, palynology; SED, sedimentology; XRF, XRF core scanning.

Sedimentology

Cores PG-51 and PG-104 were subsampled at 2-cm intervals for sedimentological analyses including carbonate content, total organic matter (TOM) and grain size. After removing carbonate content and eliminating organic matter, grain size was measured using a Horiba Laser Particle Size Analyzer at INIOAS (Nagashima et al., 2004).

TOM, total organic carbon, C/N and carbonate content

TOM was measured at INIOAS by adding hydrogen peroxide (H_2O_2) to the sub-samples of cores PG-104 and PG-51. To do this, the samples were dried in an oven at 60 °C before and after adding hydrogen peroxide. The difference in weight of the dried samples before and after the digestion was considered as the TOM content (Parker, 1983). The carbonate content of all sub-samples was measured for cores PG-51 and PG-104 using a De Bernard calcimeter.

Measurements of total organic carbon (%TOC) and total nitrogen (%TN) sedimentary content as well as the estimation of calcium carbonate content (%$CaCO_3$) were performed on 13 samples (core PG-104) of freeze-dried sediments using a Fisons Instruments Carlo Erba NA-1500 NC Analyzer at CEREGE Laboratory following the procedure described in Verardo et al. (1990). %TOC and %TN were measured after sequential addition of 0.5 M HCl to remove sedimentary carbonates, and the samples were rinsed with distilled water to neutralize the samples. %TC was also estimated through measurements without the decarbonation step. A reproducibility of ~5% for C and N content was monitored using repeated analysis of an acetanilide standard. Calcium carbonate content was then estimated for 13 sub-samples of PG-104 using the equation:

$$\%\mathrm{CaCO_3} = \left(\%\mathrm{TC} - \%\mathrm{TOC}\right) \times 8.\ 33$$

as %TC and %TOC have been measured precisely.

X-ray fluorescence core scanning

X-ray fluorescence (XRF) core scanning was conducted on cores PG-51S and PG-104 using an ITRAX core scanner (Cox Analytical Systems) at CEREGE. The relative abundances of Si, Cl, K, Ca, Ti, Cr, Mn, Fe, Br and Sr were measured by X-ray excitation using an Mo-source tube set at 30 kV and 45 mA for 15 s with a resolution of 1 and 5 mm for PG-51S and PG-104, respectively.

Downcore XRF data may vary with changes in sedimentary inhomogeneities such as pore water content and physical properties, as referred to the matrix effect (Tjallingii et al., 2007; Weltje and Tjalligii, 2008). For statistical analysis of the XRF data of cores PG-51S and PG-104, we used the Xelerate software (Weltje et al., 2015), which performs a centered log-ratio (CLR) transformation of XRF element intensities, before conducting a principal component analysis (PCA).

Organic geochemistry

Organic geochemistry analysis was carried out on 22 subsamples of core PG-51 at CEREGE. About 2 g of freeze-dried and homogenized sediment was extracted with an accelerated solvent extraction system (ASE350; Thermo Scientific) using an extraction temperature of 120 °C, a pressure of 100 bars and a mixture of dichloromethane/methanol (DCM/MeOH v/v: 9/1) as the extraction solvent.

Gas chromatography (GC) analyses were performed using an FID-equipped Thermo Scientific Trace GC device, a 60-m × 0.25-mm × 0.1-μm non-polar fused silica column (DB-5-MS; J&W) fitted with a 2.5-m × 0.53-μm deactivated retention gap and using hydrogen as the carrier gas. GC oven parameters were 45–200 °C at 17 °C min^{-1}, 200–250 °C at 5 °C min^{-1} and 250–300 °C at 3 °C min^{-1}. Concentrations of biomarkers such as alkenones and *n*-alkanes were determined by comparing with an internal standard (ethyl triacontanoate).

In addition, we calculated the *n*-alkane carbon preference index (CPI) which is the ratio of odd over even homologues (CPI = ([C27] + [C29] + [C31])/([C26] + [C28] + [C30])) modified after Bray and Evans (1961).

Palynology

In total, 12 samples were taken from core PG-51 for pollen analysis at 10-cm intervals. Samples were processed using the standard pollen extraction technique (Faegri and Iverson, 1975), avoiding treatment with NaOH. Samples were treated with 10% HCl (24 h) followed by 48% HF (24 h) and re-treated with warm (70 °C) and concentrated (37%) HCl for 15 min. After removing the mineral part, the remaining organic-rich pellet was acetalized for 5 min. The fraction size between 10 and 160 μm was mounted on the slides for microscopic identification. As samples were treated by acetolysis, which is destructive to dinoflagellate cysts, pollen analysis was limited to pollen and spores and some non-pollen palynomorphs (NPPs). Pollen identifications were aided by using pollen atlases for Europe, the Mediterranean and Africa and the pollen reference collection of Persia and Arabia hosted at Institut Méditerranéen de Biodiversité et d'Ecologie (IMBE). Microcharcoal particles larger than 10 μm found in the palynological slides were counted at IMBE laboratory. Microforaminifera and microcharcoal percentages were calculated based on the total pollen sum.

Radiocarbon dating

Based on the changes in visible sedimentological properties of the PG-51 and PG-104 cores, seven bivalve shells were collected and shipped to Beta-Analytics laboratory in Miami, USA, and Poznan Radiocarbon Laboratory in Poland for radiocarbon dating (Table 2). The available bivalve shells were a mixture of *Hecuba scortum*

Table 2. Radiocarbon age results for the studied core, their raw data and calibrated age for 1σ; a $\Delta R = 46 \pm 53$ years (1σ) was applied to all samples based on Southon et al. (2002).

Core ID	Sample	Depth (cm)	Lab. no	Material	Conventional radiocarbon age	Calibrated age (BP), median probability	68.3% (1σ) (BP)
PG-51	PG-51-1	5.5	Beta-408009	Bivalve shell	3390 ± 30	3017	3131–2912
	PG-51-2	19	Aix-10695.1.1	*Hanzawaia boueana*	2820 ± 80	2332	2471–2171
	PG-51-3	22	Aix-10695.1.2	*Hanzawaia boueana*	3000 ± 80	2551	2695–2426
	PG-51-4	27	Beta-426291	Bivalve shell	8450 ± 30	8783	8901–8653
	PG-51-5	55	Beta-426292	Bivalve shell	8980 ± 30	9442	9528–9364
	PG-51-6	122	Beta-408010	Bivalve shell	9850 ± 40	10588	10716–10469
PG-104	PG104-1	44.5	Poz-94411	Bivalve shell	3620 ± 35	3302	3401–3202
	PG104-2	81.5	Poz-94412	Bivalve shell	5520 ± 40	5661	5758–5559
	PG104-3	119.5	Poz-94413	Bivalve shell	6400 ± 40	6604	6709–6495

(Linnaeus, 1758), *Tellina* sp., *Kellia* sp., *Dosina* sp. and *Mactra* sp. On the basis of four initial radiocarbon results in core PG-51, we refined the age control with two additional radiocarbon datings performed on the benthic foraminiferal species *Hanzawaia boueana* at 19 and 27 cm using the AixMICADAS radiocarbon at CEREGE (Bard et al., 2015). The small size of the foraminiferal samples (<1 mg) led us to use the gas ion source of AixMICADAS coupled to its carbonate hydrolysis system for online leaching (Fagault et al., 2019; Tuna et al., 2018). Only one data point for the local marine reservoir age (MRA) is currently available for the PG region, indicating a ΔR of 46 ± 53 years (Reimer and Reimer, 2001; Southon et al., 2002). An age–depth relationship was created with the 'clam' package in R-Studio, Version 1.3.1093, using Marine20 (Heaton et al., 2020). The Marine20 calibration is based on a global MRA correction for the mid- to low-latitude open seas such as the PG. Finally, MS measurements performed on both PG-51 and PG-51S were used to correlate both twin cores and attribute a radiocarbon chronology to the latter core (Supporting Information Fig. S1). Table 2 summarizes all radiocarbon ages obtained on cores PG-51 and PG-104.

Results

Chronology and age–depth model

Core PG-51

Calibrated radiocarbon ages reveal a distinct discontinuity at 27 cm (Fig. 2a). According to our age–depth model, the sedimentation rate from the core's base to 27 cm depth is ~0.5 mm a^{-1} (Fig. 2a). The apparent hiatus identified at 27 cm spans around 6000 years, indicative of a period during which sediments either failed to accumulate or were disrupted by sedimentological processes. The upper section of the sediment core shows significant variations in grain size without any discernible trend and its sediments have a dark gray color. The ages in this upper 27-cm segment span from about 2.3 to 3 ka cal BP, with apparent age inversion and large uncertainties (Fig. 2a), indicating a mixed layer. As a precaution, any interpretation of diverse proxies should be confined to the interval between the core base and 27 cm, where chronological order is maintained.

Core PG-104

Three calibrated radiocarbon ages are in sequential order in PG-104, enabling us to reconstruct an age–depth model for the sedimentary sequence (Fig. 2b). According to the model, sedimentation rate changes from ~40 cm ka^{-1} at the base to ~13 cm ka^{-1} at the core top.

Sedimentology

Core PG-51

Grain-size analyses reveal that the terrigenous sediment consists predominantly of silt. Visual examination of both twin cores delineates three distinct sedimentological units (Fig. 2). The lower Unit-I exhibits homogeneity, with a relatively consistent carbonate content of ~30%. Unit-II in the middle displays a noticeable transition to a light gray color (Fig. 2). The upper contact between Unit-II and Unit-III is well defined, marked by a drop in $CaCO_3$ content from a peak of 38% to values consistently below 30% along Unit-III. Unit-III encompasses the uppermost section of the core, featuring a dark gray silt sediment layer that extends to the core top. Notably, there is an increase in sand content, reaching 10% at the core top.

TOM content ranges from 7.5 to 13.3% with an average value of 9.6%. TOM has the highest values in the darker Unit-III (Fig. 2). MS values attain their minimum in Unit-II, which mirrors the concomitant maximum recorded in the carbonate content. Grain size varies along the core concordant with the carbonate content (Fig. 2).

Given the reversal ages of Unit-III, it was excluded from our interpretation. Consequently, only the sedimentological findings of Units-I and II have been juxtaposed against age, specifically within the calibrated timeframe of ~10.9 to ~8.7 ka cal BP. This approach facilitated the identification of three distinct temporal zones delineating changes in sedimentological properties (Fig. 3). The initial zone, denoted as Zone-A_{sed}, spans from 10.9 to ~10.1 ka cal BP (Fig. 3). Most of the variables in this zone are in steady state. Grain size oscillates around 6 μm, carbonate content slowly increase from 28 to 31% and sand is nearly absent. TOM constantly decreases in tandem with MS values.

The second zone (Zone-B_{sed}) extends from ~10.1 to ~ 9.5 ka cal BP and is characterized by the lowest values of mean grain size, concomitantly with the highest sand content of the core (up to 18%), suggesting different modes of sedimentary deposition. A general fining-upward trend can be observed from the A_{sed} to B_{sed} zones, which shifts to a coarsening-upward trend in Zone-C_{sed}. On the other hand, carbonate content and TOM reach their lowest values, indicating a possible inverse relationship with the sand content.

The most distinctive changes are found in Zone-C_{sed}, centered on ~9 ka cal BP. Here the carbonate content and mean grain size reach their highest values while MS values drop to their minimum around 9 ka cal BP. Sand content is less than 5% and TOM increases around 9 ka cal BP.

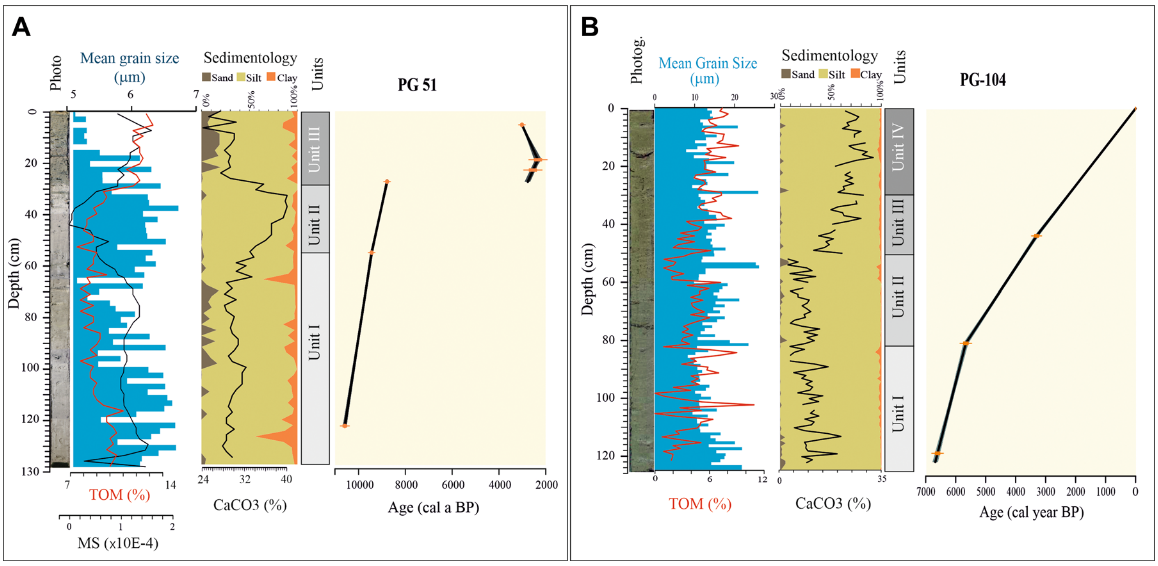

Figure 2. Age–depth models of sediment cores PG-51 (A) and PG-104 (B), displaying sedimentological properties with depth. Mean grain size (µm) is represented by blue bars, total organic matter by red lines and magnetic susceptibility (MS) for PG-51 as a black line on the mean grain size graph. Carbonate content is included on the sedimentology graph for both cores. Cores are classified into sedimentological units (I to IV) based on contrasting properties with depth. [Color figure can be viewed at wileyonlinelibrary.com]

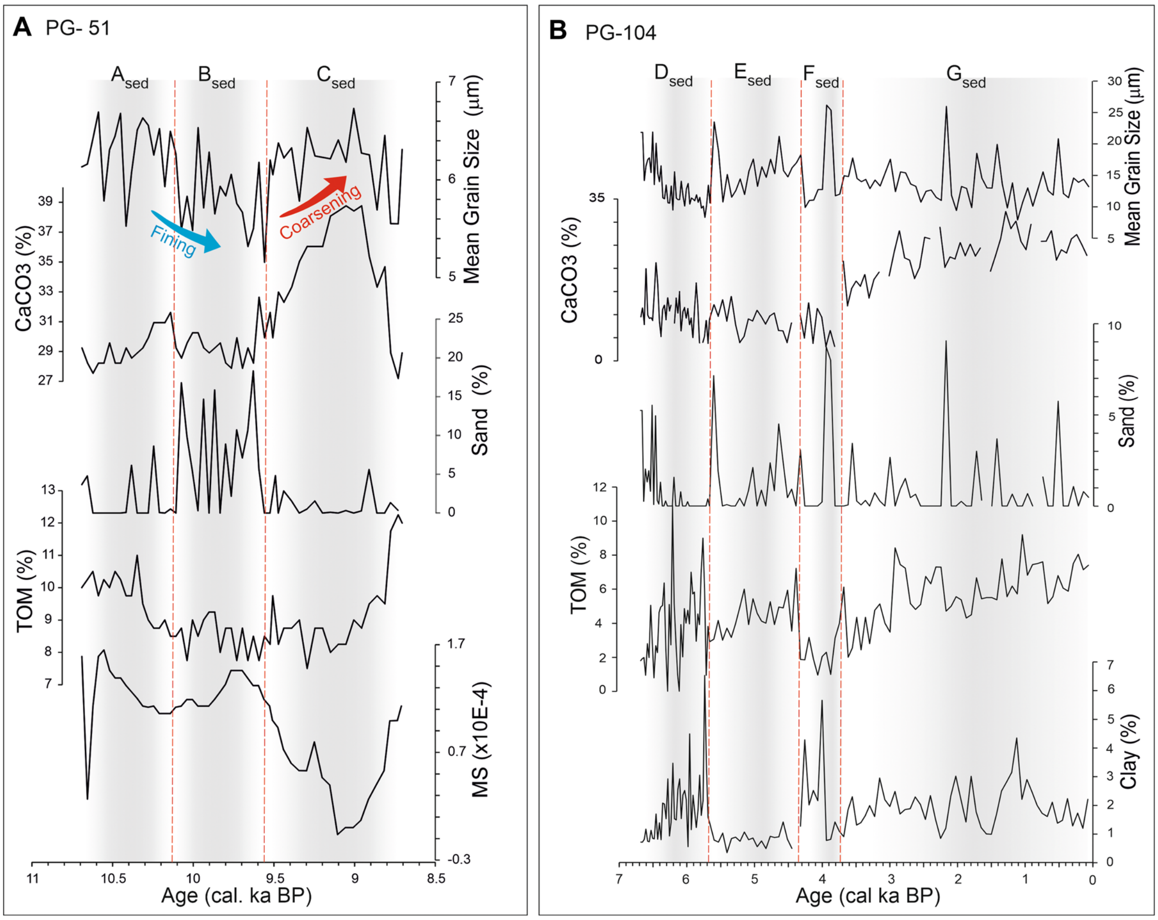

Figure 3. Variation of sedimentological properties of core PG-51 (A) and PG-104 (B) with age. Correlated zones are indicated by shaded zones and labeled 'A_{sed}' to 'D_{sed}'. The borders of the zones are indicated by dashed lines. [Color figure can be viewed at wileyonlinelibrary.com]

Core PG-104

Core PG-104 consists predominantly of silt with little visual variation. However, a nuanced categorization reveals four distinct temporal zones of sedimentological alterations (Fig. 3b).

Zone D_{sed}, spanning ~6.7 to ~5.7 ka cal BP, exhibits the lowest sedimentation rate, accompanied by variable clay and TOM content. Concurrently, carbonate content decreases from >20 to <5%, coinciding with a reduction in grain size (Fig. 3b).

Zone E_{sed} encompasses the period from ~5.7 to 4.3 ka cal BP, characterized by an increase in grain size and sand content, coupled with a decline in TOM and clay content.

Zone F_{sed}, spanning ~4.3 to 3.7 ka cal BP, is marked by an increase in clay, sand and mean grain size, while TOM decreases. Although carbonate remains relatively stable throughout this zone, a conspicuous step-like increase in carbonate content at the end of the zone is observed, escalating from values below 5% to over 20%.

Lastly, zone G_{sed} covers the last 3.7 ka, displaying a rising trend in TOM and carbonate content. Despite notable oscillations in mean grain size, clay and sand content, no discernible trend is evident within this zone.

XRF core scanning

PCA reveals noticeable downcore shifts in elemental clusters for core PG-51S, contrasting with the homogeneous composition of core PG-104 (Fig. 4). In PG-51S, PCA identifies three distinct clusters (Fig. 4a): (i) elements mainly associated with carbonates (Ca, Sr), (ii) elements mainly associated with pore water (Cl, Br), and (iii) elements mainly associated with the detrital phase (Fe, Ti). Conversely, for PG-104, four clusters exist: (i) Sr, Ca and Br, carbonate-associated elements; (ii) Cl, associated with pore water and grouped with Mn; (iii) elements mainly associated with the detrital phase (Fe, K, Ti); and (iv) Si, which appears to behave independently (Fig. 4b).

Core PG-51S

PC1 explains 50.8% and PC2 28.8% of the downcore XRF variations (Fig. 4). Variations of PC1 are dominated by the negative correlation between the lithogenic and carbonate elements, while PC2 mainly reflects a negative correlation between carbonate elements versus Cl and Br, which are commonly derived from pore water and organic matter, respectively. We then use Ca/(*lithogenic elements*) as a proxy for carbonate versus siliciclastic sedimentation (Fig. 5). Interestingly, core PG-51S also shows a negative correlation between carbonate elements and Br and/or Cl along PC2. As PC1 explains more than half of the variance, and Br and Cl have no load along PC1, normalizing Br or Cl with any other element would inevitably give variations strongly resembling those of elements plotted along PC1. In addition, we have used Fe/Mn as an indicator of redox conditions in the marine environment and provisionally as an indicator of water depth during the early Holocene (Pakhomova et al., 2007).

The results reveal prominent variations in the variables along core PG-51S, allowing us to categorize early Holocene changes into three temporal zones: A_{XRF}, B_{XRF} and C_{XRF} (Fig. 5a). The A_{XRF} zone extends from the beginning of the records to around ~9.2 ka cal BP and is characterized by low-amplitude changes in the variables. Notable is the emergence of significant shifts around 9.6 ka cal BP. Furthermore, the substantial alteration observed in the Br/Cl and Ca/Sr curve at 9.4 ka cal BP merits careful consideration (Fig. 5a).

Zone B_{XRF} is distinguished from the other zones by its high variability of changes (except for Br/Cl), spanning from ~9.2 to ~8.9 ka cal BP. The Ca/Fe and Ca/Si ratios attain their peak values concurrently with Fe/Mn while Ca/Sr and Ti reach minimum values.

Zone C_{XRF} spans from 8.9 ka cal BP to the end of the XRF records. This zone is marked by relatively high-frequency variations of the variables, especially around 8.8 ka cal BP (Fig. 5a). The Ca/Fe, Ca/Si and Fe/Mn curves reach their minimum values around 8.85 ka cal BP and recover to attain high values before 8.8 ka cal BP. Conversely, Ti exhibits its maximum values around ~8.85 ka cal BP with a significant drop before 8.8 ka cal BP. The high-frequency oscillations in the mentioned variables persist until the end of the records. A notable feature is the Br/Cl decline around 8.85 ka cal BP and the relatively stable condition of Ca/Sr throughout zone C_{XRF}.

Core PG-104

The PCA of geochemical variables in core PG-104 reveals that PC1 and PC2 are responsible for 36% and 22% of the XRF variations, respectively (Fig. 4). These principal components display consistent variations along the core, indicating a

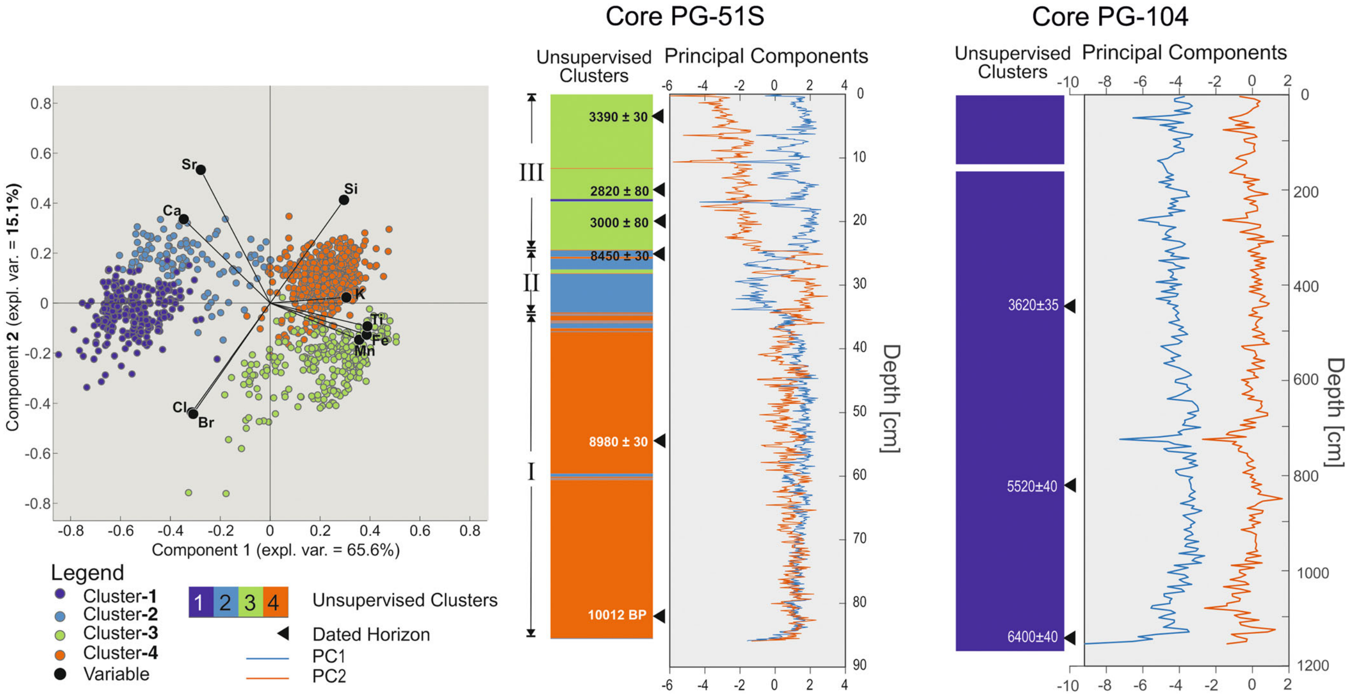

Figure 4. The results of principal component analysis (PCA) and cluster analysis for XRF data of cores PG-51S and PG-104. [Color figure can be viewed at wileyonlinelibrary.com]

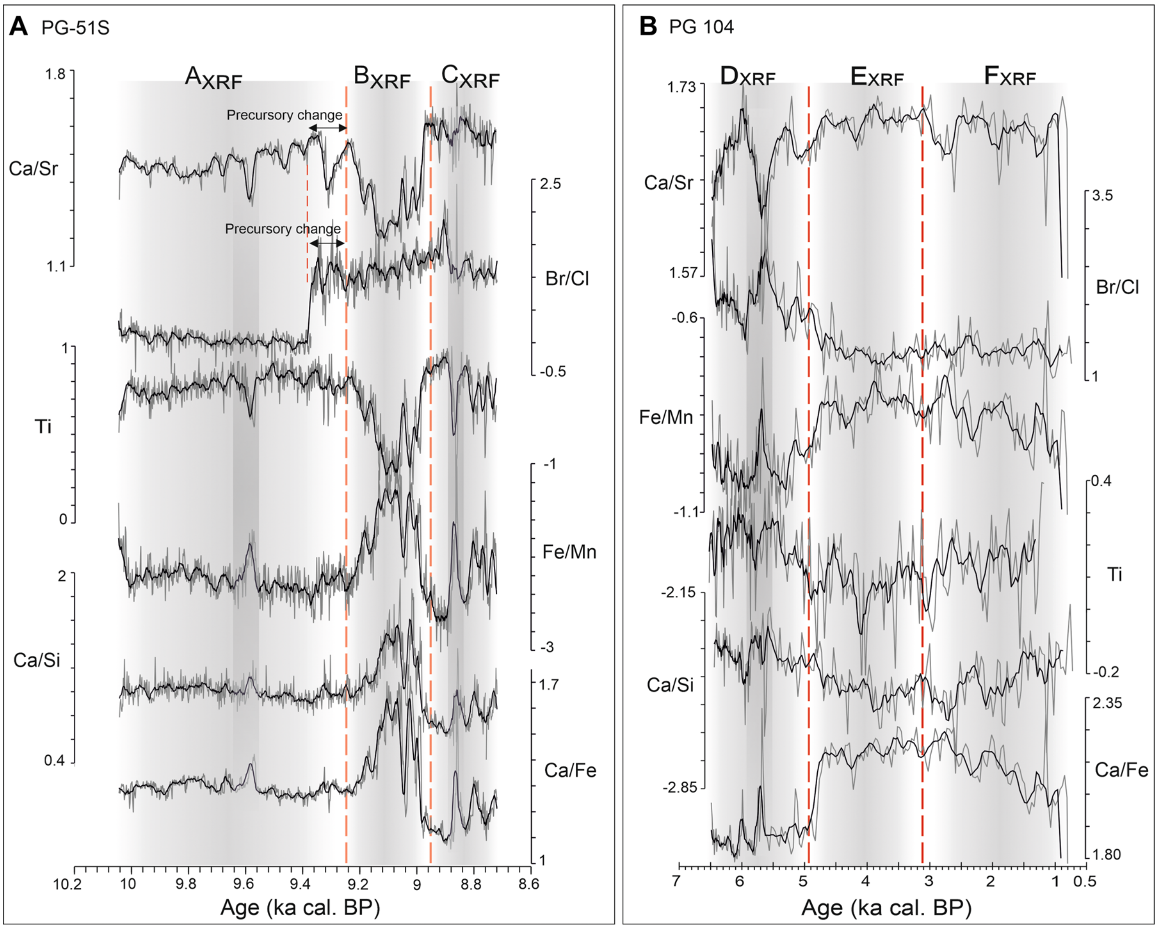

Figure 5. Variations in elemental ratios for cores PG-51S (A) and PG-104 (B). Each core shows three distinct zones of temporal changes in elemental ratios, labeled A_{XRF}, B_{XRF} and C_{XRF} for PG-51S, and D_{XRF}, E_{XRF} and F_{XRF} for PG-104. The zones are indicated by shaded areas, with darker shades representing minor, but notable, changes at 9.6, 8.9 and 5.8 ka cal BP. In A, Br/Cl and Ca/Sr ratios show notable changes before other variables that are indicated as precursory changes. The boundaries of the zones are marked by red dashed lines. [Color figure can be viewed at wileyonlinelibrary.com]

negative correlation between lithogenic and carbonate-associated elements.

Plotting Ca/(*lithogenic elements*), Ti, Br/Cl and Fe/Mn along core PG-104 reveals variations that allow us to delineate mid- to late Holocene changes into three zones: D_{XRF}, E_{XRF} and F_{XRF} (Fig. 5b).

Zone D_{XRF}, spanning from the beginning of the records to ~4.8 ka cal BP, is marked by high-amplitude changes, particularly around 5.8 ka cal BP. Ti shows a declining trend throughout this zone with a drop around 5.8 ka cal BP. Br/Cl reaches its highest values around 5.8 ka cal BP.

A distinctive increase in Ca/Fe values and a flattening of the Br/Cl curve set zone D_{xrf} apart from E_{XRF}. Zone E_{XRF} covers the temporal variation of the variables from ~4.8 to 3.8 ka cal BP, displaying relatively stable trends in all geochemical variables, except for Fe/Mn and Ti curves, which change with higher amplitudes around 4 ka cal BP.

Organic geochemistry and palynology

Organic geochemistry (core PG-51)

According to Fig. 6a, three zones, A_{bio}, B_{bio} and C_{bio}, can be distinguished based on the changes in organic geochemistry that are closely correlated with pollen counts (Fig. 6b). Zone A_{bio} is characterized by very low values of total C_{37} alkenones ($\leq 60\,\mathrm{ng\,g^{-1}}$), low values of C_{31}/C_{29} ratio (≤ 0.8), CPI ≤ 1.5 and total *n*-alkanes reaching ca. $1200\,\mathrm{ng\,g^{-1}}$. This zone extends from the beginning of the records to ~10 ka cal BP.

Zone B_{bio} is limited between ~10 and ~9.2 ka cal BP and indicated by low C_{37} alkenone values, an increasing trend of C_{31}/C_{29}, fluctuations of CPI around 1 and total *n*-alkanes reaching their maximum value.

Zone C_{bio} is differentiated by a distinct rise of C_{37} alkenones, accompanied by increasing CPI and C_{31}/C_{29} values from 9.2 ka cal BP to the end of the record.

C and N results (core PG-104)

Values of C (C_{org} and C_{total}) and N generally increase from the core base to the top (Fig. 7). C_{org}/N varies from >7 to <14, and $CaCO_3$ ranges between >77 and <83%. Total carbon (C_{total}) and $CaCO_3$ exhibit synchronous oscillations. Fluctuating values with time categorize CN measurements into three temporal zones: D_{bio}, E_{bio} and F_{bio} (Fig. 7).

Zone D_{bio} spans from the core base to ~5 ka cal BP. $CaCO_3$ decreases to a minimum around 5.7 ka cal BP, while C_{org}/N peaks around this time. C/N ratio shows a continuous increase throughout the zone.

Zone E_{bio} is limited to between ~5 and ~3 ka cal BP. At the D_{bio} to E_{bio} transition, C_{org}/N values drop sharply and continiue with a declining trend to the end of the record. $CaCO_3$, which reached its lowest values in zone F_{bio}, show a change in trend to gain its highest values around 3.8 ka cal BP, in accordance with C_{org} values. %N continue its linear increase that started from the beginning of the record. C_{org}, after a drop around 5 ka cal BP, rebounds and increases towards the end of the zone.

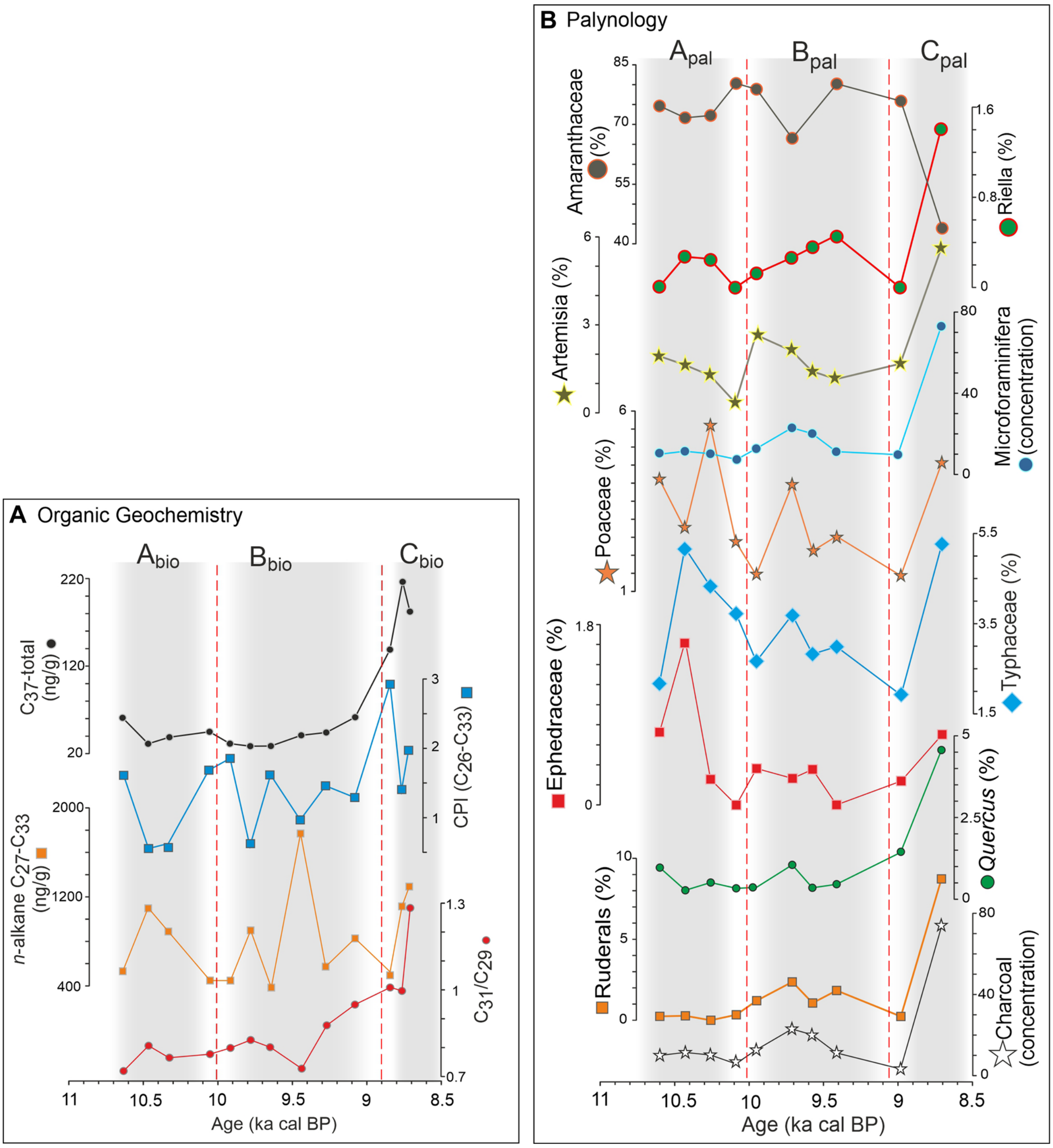

Figure 6. Results of organic geochemistry analysis (A) and palynological studies (B) of core PG-51. The results are correlated in the three shaded zones of A, B and C. The zonations for the two proxies are differentiated by the subscripts 'bio' and 'pal' for organic geochemistry and palynology, respectively. [Color figure can be viewed at wileyonlinelibrary.com]

In zone F_{bio} (from ~3 ka cal BP to the end of the record), $CaCO_3$ and C_{org}/N ratio exhibit a decreasing trend, C_{total} does not change meaningfully, while C_{org} and N values steadily increase.

Pollen analysis (core PG-51)

For core PG-51, based on changes in selected pollen taxa (from 33 identified pollen taxa) and NPPs, we identified three palynological zones: A_{pal}, B_{pal} and C_{pal} (Fig. 6b). We selected the pollen taxa that are ecologically significant and indicative of the general paleoecological changes in the PG basin, and that supplement the other proxy data in our study. We did not focus on upland taxa, except for *Quercus*, as they have diverse sources. Instead, we examined those taxa that indicate the vegetation (hydrology) of the PG and its surroundings. For instance, we present the variation in pollen of the family Amaranthaceae as the most prevalent pollen type. This family is mostly xerophytic and salt-tolerant. Its pollen percentage ranges from ~40% to ~85%, indicating shifts in soil salinity and climate aridity in the PG basin during the early Holocene. These pollen data complement the other proxy data in our study.

According to the recognized zones, zone A_{pal} (~10.7 to ~10 ka cal BP) is distinguished by high pollen percentages of desert shrubs (Ephedraceae) and higher pollen percentage of Amaranthaceae. Within this zone, wetland pollen types (Typhaceae and *Riella*) display varying but notable values. Microforaminifera exhibits lowest concentrations in this zone.

In zone B_{pal} (~10 to ~9.2 ka cal BP), the Amaranthaceae curve shows a trough around 9.7 ka cal BP but the percentage remains high. *Riella* shows a constant increase during this time, while *Artemisia* declines. Microforaminifera concentration increases slightly in zone B_{pal}. In this zone, there is a concurrent rise in Poaceae, Typhaceae, *Quercus*, ruderals and microcharcoal, coinciding with a decrease in Ephedraceae.

In zone C_{pal}, each variable has one data point. However, it is evident that Amaranthaceae declines by two-fold, whereas oak and wetland pollen increase modestly. Microcharcoal

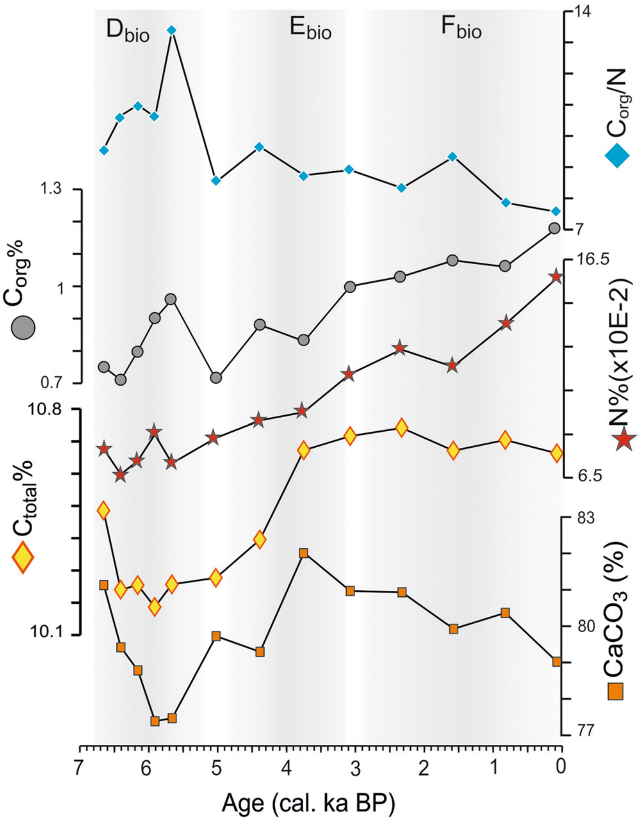

Figure 7. The results of carbon and nitrogen (CN) measurements for core PG-104. Three different zones (D$_{bio}$, E$_{bio}$ and F$_{bio}$) are distinguished and indicated by shaded zones and labels. [Color figure can be viewed at wileyonlinelibrary.com]

percentage rises, and there is an upsurge in ruderals, especially *Plantago lanceolata*-type pollen.

Discussion

The dilemma of the Holocene hiatus

In this study, radiocarbon ages of benthic foraminifera in core PG-51 are consistent but younger than the topmost age from bivalves (Table 2). The age–depth model indicates an apparent hiatus postdating 8.7 ka cal BP (Fig. 2a). Two plausible scenarios explain this: (i) a catastrophic event removing early to late Holocene sediments; or (ii) prolonged oceanographic conditions (e.g. strong currents) hindering or winnowing sedimentation.

Late Holocene sea level was similar to the present (Lambeck, 1996). As a result, to remove early to late Holocene sediments from the sea floor in our study area, an extraordinary event such as tsunami is required, as slope failure is unlikely due to the flat topography of the study area (Fig. 1). Regarding tsunamis, the shallow PG basin is less prone to experiencing powerful earthquakes (Nowroozi and Ahmadi, 1986) and hence the prospect of tsunamis originating from seismogenic sources within the PG is unlikely (Heidarzadeh et al., 2020). The morphology of the Strait of Hormuz prevents distal tsunami waves from the Gulf of Oman affecting the PG (Heidarzadeh et al., 2020). While other sources such as meteotsunamis occur in the shallow coastal waters of the PG, they do not affect deeper areas (Heidarzadeh et al., 2020). Moreover, the absence of soft sediment deformation in the cores suggests no evidence of seismic activity-related impacts, ruling out paleoseismic deformations such as liquefaction.

The suggestion of a sediment hiatus due to oceanographic conditions lacks support from other PG paleoceanographic investigations (Hosseinyar et al., 2021; Lambeck, 1996; Purser, 2012; Uchupi et al., 1999). If stronger sea currents were responsible for sediment removal, one would anticipate basin-wide evidence, which is not found in these studies. Moreover, insights from the PG-104 core in this study indicate continuous sedimentation in study area, persisting since ~6.7 ka cal BP.

The most likely explanantion for the discrepancy is bioturbation processes. Bioturbation transports small particles, such as foraminiferal tests, vertically (Leuschner et al., 2002). This explains why the upper three radiocarbon dates, with two based on a minimal number of benthic foraminiferal shells, show random late Holocene ages (Dolman et al., 2021). Despite a low bioturbation rate in the deep PG waters (Behbahani et al., 2015), it can still mix small particles, blending older and younger horizons (Purser, 2012). Consequently, we interpret the upper part of the PG-51 core as a mixed, bioturbated layer and have excluded it from our interpretations.

Persian Gulf during the Early Holocene

Climatic changes and vegetation history

Around ~10.2 ka cal BP, the IOSM strengthened in terms of wind intensity (Gupta et al., 2003) (Fig. 8l). Concurrently, the Westerlies jet was positioned at its highest latitudes during the Holocene (Fig. 8n), and dry conditions prevailed in the northwest of Iran and probably the northern PG catchment basin (Sharifi et al., 2015; Sharifi et al., 2018). The study area was also experiencing drier conditions at this time, as attested by high pollen percentages of desert shrubs (Ephedraceae) and the highest pollen percentages of Amaranthaceae from ~10.7 to ~10 ka cal BP. The dominance of Amaranthaceae may indicate that the exposed surface of the WSB and adjacent areas were dominated by members of the family Amaranthaceae, which includes both halophytic/halotolerant and non-halophytic species (Akhani, 2006). Most species of this family are well adapted to desert environments and saline soils and salt marshes (Akhani, 2006; Djamali et al., 2012). At the same time, the wetland pollen types (Typhaceae and *Riella*) display varying but notable values, showing that sea-level fluctuations at the beginning of the Holocene (Liu and Milliman, 2004) controlled the position and extent of wetland systems with respect to the coring site. This condition is supported by an increase of carbonate content around 10.4 ka cal BP (Fig. 8e), rise in Fe/Mn and Ca/Fe around 9.6 ka cal BP (Fig. 8a and D) and an upsurge in Br/Cl values around 9.4 ka cal BP (Fig. 8c).

It appears that the early Holocene climatic change was accompanied by the major phase of PG transgression that occurred around 9.2 ka cal BP when C_{37}-total, as an indicator of a marine environment (Castañeda and Schouten, 2011), increased to the end of the record (Fig. 8g). This is corroborated by the distinct rise in microforaminiferal frequency (Fig. 8h).

Although long-chain *n*-alkanes can be produced in marine environments by different species of algae (Conte et al., 1994; Volkman et al., 1995), they are mainly synthesized by terrestrial plants that are then transported by wind and/or river systems into marine environments (Vogts et al., 2012). In many environments, the chain length of *n*-alkanes in plants is mainly controlled by temperature and/or aridity (Bush and McInerney, 2015; Seki et al., 2021). C_4-type plants (grasses) are common in hot and dry environments and exhibit distribution maxima in C_{31}- or C_{33}-alkanes (Meyers and Ishiwatari, 1993). By contrast, C_3-type plants (woody plants) exhibit distribution

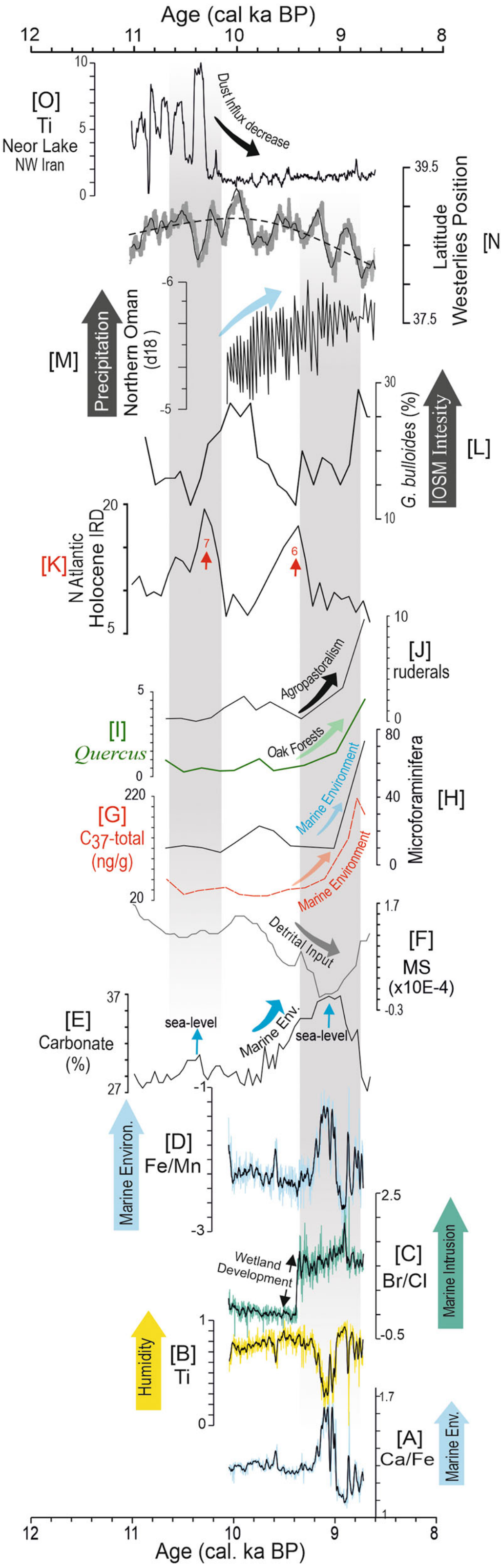

Figure 8. Early Holocene environmental changes in the Persian Gulf and other regional and global changes. Panels A–J present findings from this study, with arrow-annotated interpretations. (K) Holocene ice-rafted debris (IRD) events (Bond et al., 1997); (L) the frequency of *Globigerina bulloides* in Arabian Sea sediments (Gupta et al., 2003); (M) δ^{18}O changes in a Hoti Cave stalagmite in northern Oman (Fleitmann et al., 2003); (N) reconstructed position of the MLW jet during the Holocene based on the NCARModel (Sharifi et al., 2018); and (O) Ti intensity curve in Neor Lake sediment core in northwest Iran (Sharifi et al., 2015). Shaded zones denote correlations between our study results and global/regional changes. [Color figure can be viewed at wileyonlinelibrary.com]

maxima in C_{29} or C_{31} (Meyers, 2003; Rommerskirchen et al., 2006; Vogts et al., 2012). We thus use the C_{31}/C_{29}-alkane ratio as a proxy for vegetation adaptation to climate conditions (Vogts et al., 2012; Leider et al., 2013; Horikawa et al., 2010), with higher values corresponding to drought-adapted vegetation and lower values to vegetation adapted to more humid conditions. Moreover, the CPI provides an index to distinguish fresh (with high CPI) from degraded terrestrial organic matter (with low CPI) (Bray and Evans, 1961, Eglinton and Hamilton, 1967; Castañeda and Schouten, 2011). Based on the above, the low values of CPI and C_{31}/C_{29} before ~9.2 ka cal BP indicate that reworked and altered terrestrial organic material was transported to the WSB by rivers or winds (Vogts et al., 2012). By contrast, after ~9.2 ka cal BP, higher CPI and C_{31}/C_{29} values indicate fresher terrigenous organic material input to the WSB during a more humid climate period, allowing vegetation to grow in proximity to the PG. The more humid climate in the study area is supported by speleothem stable isotope evidence from northern and southern Oman that suggest IOSM precipitation increased (Fig. 8m), due to northward propagation of the ITCZ (Fleitmann et al., 2007). At this time southeastern Iran was receiving higher dust influxes due to a more intense IOSM in terms of wind strength (Safaierad et al., 2020). However, the southern PG drainage basin in the Arabian Peninsula was more influenced by the IOSM in terms of precipitation (Parker et al., 2004). Palchan and Torfstein (2019) showed that dust influx was reduced by at least two-fold during the African Humid Period from the early to mid-Holocene. The same condition is reported from Arabia by an evident decline in Ti records (Parker et al., 2006). The PG sediments evidently show this decline in Ti input as a sign of major regional climatic change from drier to more humid conditions (Fig. 8b). As a result, the regional vegetation would have changed from xerophytic desert vegetation to grass steppes (Parker et al., 2004). Halophytic taxa, including Amaranthaceae, reached their minimum extent consistent with the disappearance of continental sabkha environments and saline soils (Parker et al., 2006).

From ~9 ka cal BP, Amaranthaceae declined, and oak pollen increased slightly (Fig. 8i) along with wetland-type pollen and microcharcoal percentages, suggesting that the Zagros oak woodland expanded and wetlands developed around the WSB (Fig. 8c). The coeval increase in trees, shrubs and grasslands recorded in our studied core supports the findings of Parker et al. (2004, 2006) on the development of true savanna-like ecosystems in the study area. Due to vegetation and soil development, dust sources were restricted and aeolian input declined, as attested by the declining frequencies of Ti (Fig. 8b). Simultaneously, agropastoral activity increased by 9.2 ka cal BP (Fig. 8j), supported by an increase in ruderals, mainly *Plantago lanceolata*-type pollen (Bottema and Woldring, 1990; Djamali et al., 2009). It appears that at this time a flourishing upstream vegetation was responsible for more human activity and the high amount of ruderal pollen. Microcharcoal percentage is a proxy for fire episodes that are, in turn, linked to the development of continental grasslands and grass steppe vegetation. Denser vegetation could be responsible for more landscape burning, reflected in the highest percentages of microcharcoal in our records.

Persian Gulf flooding

The characteristics of the study site, including the presence of wetland plants (e.g. Typhaceae), CPI ≤ 1, relatively high organic carbon content, a notable distribution of *n*-alkanes and the existence of marine bivalves, suggest that the WSB experienced inundation prior to 9.2 ka cal BP, resembling an estuarine/deltaic environment (Sholkovitz, 1978). The deltaic nature is further supported by the observed upward-fining trend in sediment grain size (Fig. 3a).

According to Liu and Milliman (2004) and Smith et al. (2011), the key phases of deglacial global sea-level rise occurred approximately at 14, 10.5 and 9 ka BP, with corresponding sea levels reaching about −60, −40 and −20 m, respectively. Our sedimentological findings show notable variability in the sand fraction from ~10.5 to 10.1 ka cal BP (Fig. 3a). During this period, we observe a peak in carbonate content (Fig. 8e), a smooth rising trend in microforaminiferal concentration (Fig. 8h) and a slight decline in MS values (Fig. 8f). These indicators suggest that the sampling site experienced inundation during the postglacial sea-level rise around 10.4 ka cal BP when global sea level was approximately −40 m (Liu and Milliman, 2004; Smith et al., 2011). These findings align with cooling phase-7 from the North Atlantic (Fig. 8g) (Bond et al., 1997), supporting the global connection of these changes. Additionally, the paleoceanographic model of Lambeck (1996) indicates that the WSB was submerged around 11.5 ka BP, with a brief stillstand between ~11.3 and 10.5 ka BP. The subsequent phase of sea-level rise began around 10.5 ka BP, probably captured in core PG-51.

The major inundation phase of the WSB commenced around 9.2 ka cal BP and lasted for 300 years, attested by a sudden increase in the Ca/Fe ratio (Fig. 8a) and carbonate content (Fig. 8e) and a clear decline in MS values (Fig. 8f). This shift indicates a rise in marine carbonate production and a reduction in terrestrial inputs, supported by a decrease in Ti intensity (Fig. 8b). The increased biogenic carbonate production, characterized by a notable increase of Sr and Ca, suggests a transition to a deeper marine environment, primarily attributed to aragonite shells of marine invertebrates (Richter et al., 2006).

Additional evidence supporting PG flooding at 9.2 ka cal BP is found in the C_{37}-alkenone concentration (Fig. 8g). Notably, the upper 30 cm of core PG-51 exhibits C_{37}-alkenone values exceeding 200 ng g^{-1} (data not shown due to radiocarbon date discrepancies), suggesting a marine environment after 8.8 ka cal BP. C_{37}-alkenones are mainly found in marine sediments, where they are synthesized by haptophyte algae, such as coccolithophores (Brassell et al., 1986). However, these alkenones can also occur in other environments such as lakes (Thiel et al., 1997; D'Andrea et al., 2006; 2013) and brackish environments (Schwab and Sachs, 2011), where some freshwater haptophytes can produce C_{37}, C_{38} and C_{39}-alkenones. Nevertheless, C_{37}-alkenones are very abundant in marine environments, and the C_{37} unsaturation ratio is commonly used as a proxy for sea-surface temperature (Prahl et al., 1989). It is worth noting that some alkenones can also be transported by marine aerosols (Sicre et al., 1990). However, the notable increase of C_{37}-alkenones along with other evidence indicates the formation of a marine environment since 9.2 ka cal BP (Fig. 8g).

The Br/Cl ratio (Fig 8c) also increased at 9.2 ka cal BP, further confirming a notable marine intrusion at this time. Elevated percentages of carbonate, increased organic matter and reduced detrital input collectively contributed to a decline in MS values (Fig. 8f). Additionally, microforaminiferal concentration started to rise at an accelerating rate during this period (Fig. 8h).

Before the establishment of a definitive marine environment, the depositional conditions at the study site resembled today's ASH (Fig. 1), characterized by predominant carbonate deposition (Purser, 2012). With deepening seas, the general circulation of the PG became established (Hamzeh et al., 2021; Hosseinyar et al., 2021; Lambeck, 1996). Tidal and wind forces reinforced deepened water currents (Pous et al., 2012; 2013), leading to the transport of fine-grained sediments and a reduction in sedimentation rates in the WSB. The main phase of sea-level rise that started 9.2 ka cal BP eventually transformed the sedimentary environment of the sampling site into its present-day conditions after 8.8 ka cal BP, with the top 30 cm of dark-colored sediments deposited during a new phase of lower sedimentation rates.

Persian Gulf during the mid- to late Holocene

Core PG-104 proxy records reveal significant variations from 6.7 ka cal BP, with the period between 6.3 and 4.8 ka cal BP displaying pronounced changes (Fig. 9). These variations correspond to a notable climatic event in the Northern Hemisphere during the mid-Holocene, centered approximately on 6.3 ka ago (Taylor et al., 2018). During this event, weakening of the IOSM and strengthening of the MLW were observed (Fleitmann et al., 2007; Stevens et al., 2001; Djamali et al., 2010).

Parker et al. (2006) documented a shift from wetter to drier conditions in the southern watersheds of the PG since 6.3 ka cal BP, a change that is precisely recorded in the speleothems from Oman (Fig. 9i) (Fleitmann et al., 2007). The North Atlantic cooling phase-4 (Fig. 9g) probably induced stronger Westerlies at higher latitudes, leading to a significant increase in dust influxes from ~6.5 to 5 ka cal BP in Lake Neor, NW Iran, peaking around 5.8 ka cal BP (Fig. 9k) (Sharifi et al., 2018). The pronounced North Atlantic climatic control and strengthening of zonal Westerlies led to wetter conditions in southern Europe (Taylor et al., 2018). This episode is reflected in the PG with much higher C_{org}/N ratio values (Fig. 9e). The C/N ratio is commonly used to differentiate terrestrial from marine sources of organic matter in sediments (Perdue and Koprivnjak, 2007). Terrestrial organic matter, depleted in nitrogen, contrasts with nitrogen-enriched marine-derived organic matter. Lower C/N ratios indicate a higher contribution from marine sources, while higher values signify terrigenous organic matter sources. As a result, it appears that the PG experienced an enhanced influx of terrestrial organic matter during the mid-Holocene, which declined significantly during the late Holocene (Fig. 9e). The mid-Holocene is also indicated as a sedimentary phase with an increased clay fraction (Fig. 9f). Enhanced clay content may sequester nutrients in marine settings, preventing eutrophication and lowering nitrogen levels in the sediments (Xu et al., 2013). This may be an additional mechanism for nutrient removal and eutrophication inhibition in the PG, resulting in higher C_{org}/N ratios (Fig. 9e).

The lowest Fe/Mn values during this period suggest more suboxic/anoxic conditions in the basin (Calvert and Pedersen, 1992), preserving more organic carbon in the sediments (Fig. 9e). This is supported by highest values of Br/Cl as a proxy for organic content of sediments (Ziegler et al., 2008) (Fig. 9d). Suboxic conditions in the modern PG are also reported by Saleh et al. (2021), occurring during summer to autumn mainly at depths ≥50 m. The authors demonstrated that hypoxic conditions have affected more areas of the PG under ongoing climate change. During the mid-Holocene, the heightened suboxic/anoxic conditions in the PG led to a decline in $CaCO_3$ production, clearly seen in the lowest Ca/Fe and $CaCO_3$ values during this episode (Fig. 9c and A). The reduction in Ca/Fe ratio, as an indicator of intra- to extrabasinal sediment provenance, can be attributed to an intensified detrital influx into the basin, probably by wind. This is corroborated by the observed increase in the clay fraction in the sediment composition (Fig. 9f).

The 6.3-ka climatic event coincides with the southward migration of the Westerlies jet position (Fig. 9j) and the ITCZ

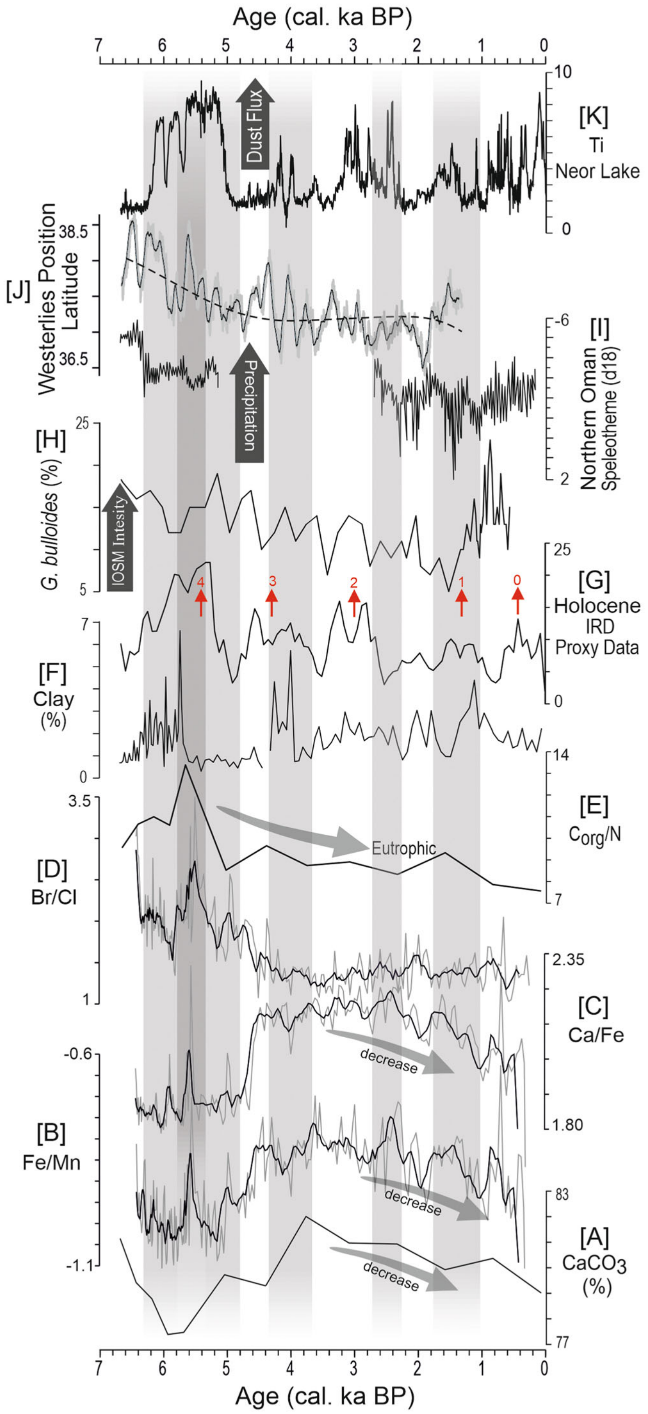

Figure 9. Mid- to late Holocene environmental shifts in the Persian Gulf, coupled with regional and global changes. Panels (A–F) are the results of this study, with arrow-annotated interpretations for some. (G) Holocene ice-rafted debris (IRD) events (Bond et al., 1997); (H) the frequency of *G. bulloides* in Arabian Sea marine sediments (Gupta et al., 2003); (I) $\delta^{18}O$ log changes in a stalagmite from Hoti Cave in northern Oman (Fleitmann et al., 2003); (J) reconstructed position of the MLW jet during the Holocene based on the NCARModel (Sharifi et al., 2018); and (K) Ti intensity curve in a sediment core from Neor Lake in northwest Iran (Sharifi et al., 2015). Shaded zones indicate correlations between our study results and global/regional changes. [Color figure can be viewed at wileyonlinelibrary.com]

(Fig. 9i) (Fleitmann et al., 2007; Sharifi et al., 2018). The southward movement of the ITCZ reported by Fleitmann et al. (2007) contributes to aridification in the southern watershed of the PG (Parker et al., 2006), potentially leading to increased aeolian input into the basin. Simultaneously, the southward migration of the Westerlies jet (Sharifi et al., 2018) (Fig. 9j) results in increased moisture in the northern watershed of the PG, affecting uplands in Mesopotamia and the Zagros Mountains, and establishing the modern seasonal distribution of precipitation (Stevens et al., 2001) and vegetation cover (Djamali et al., 2008).

Following the unstable conditions resulting from the mid-Holocene climatic shift, the PG has experienced a relatively stable environment since 4.8 ka cal BP, evident in low-amplitude changes in the variables (Fig. 9). Despite this stability since 4.8 ka cal BP, minor oscillations are discernible in the PG-104 records.

A global event of extreme importance occurred from 4.3 to 3.8 ka BP, peaking around 4.2 ka BP that has been repeatedly reported in West Asia (Kaniewski et al., 2018). This event is reflected in PG records, particularly in terms of $CaCO_3$ content and clay portion of the sediments (Fig. 9a and F). The substantial increase in the clay portion may be attributed to heightened aeolian dust input during the prolonged West Asian drought (Kaniewski et al., 2018). Given the prevalence of the MLW since ca. 6.3 ka BP, the source of this aeolian dust is probably linked to Mesopotamian and Levant dust sources, west of the PG. These sources, mainly composed of carbonates from the erosion of calcareous rocks in peripheral regions, contribute to the increase in $CaCO_3$ from ~77% at ~4.8 ka cal BP to ~82% at ~3.8 ka cal BP, supporting the idea of proximal dust sources (Fig. 9a). However, inorganic geochemical variables exhibit minimal changes during the 4.2-ka event.

From 2.8 ka cal BP onward, different variables gradually decline until the end of the records (Fig. 9a–c) without substantial changes. This relatively stable paleoceanographic condition can be attributed to the region's stable climate. The sole high-amplitude change in our records corresponds to clay (Fig. 9f), showing noticeable variations between 1.8 and 1.1 ka cal BP. This episode aligns with the Late Antiquity Little Ice Age reported in the Northern Hemisphere (Büntgen et al., 2016) and correlates with cooling phase-1 in the North Atlantic (Fig. 9g). Büntgen et al. (2016) attribute the cooling event maximum to a series of large volcanic eruptions around ca. 1.4–1.3 ka BP (Fig. 9g).

Conclusions

This study has explored the sedimentary records of the semi-enclosed basin of the PG, which preserves the history of postglacial flooding events and Holocene climate changes. The PG sediments reflect not only the paleoceanographic conditions of the basin, but also the climatically induced environmental changes in the surrounding landmasses.

We have demonstrated that the western part of the PG was inundated by successive rapid transgressional phases around 10.4, 9.6 and 9.2 ka cal BP, followed by stable marine conditions after 8.8 ka cal BP. These landscape changes were synchronous with an intensification of the IOSM during the early Holocene, which led to a transformation of the vegetation in the adjacent lands. We also detected a concurrent increase in agropastoral activity around 10.4 ka cal BP, peaking from 9.2 ka cal BP, in accordance with the environmental changes.

We have shown also that the long-term sedimentary changes in the PG have been increasingly influenced by climatic events on the neighboring landmasses after the formation of the sea. The impacts of the 6.3-ka event, marked by a decrease in the IOSM intensification and a dominance of the Westerlies, are recorded in PG sediments. It appears that this climatic shift was a multiphase phenomenon that extended from ~6.7 to 4.8 ka cal BP, with the maximum changes occurring around 5.8 ka cal BP.

We observed that late Holocene regional climatic events left fewer discernible marks on PG sediments than earlier events, especially in high-resolution geochemical variables. Further investigation is needed to examine the late Holocene climatic events in the region using PG sediments. We suggest that comparing PG sediments with other regional and global records, especially terrestrial archives around the PG, will improve our understanding of climatic dynamics in this critical geographic area and its impacts on the marine environment.

This study has raised new questions about how paleoenvironmental changes affected human development in West Asia, such as the neolithization process during the early Holocene, the formation of early-states societies, and the emergence of sailing and long-distance trading during the mid-Holocene climatic shift. These socio-economic revolutions coincided with the major phases of variable changes observed in our records. Moreover, this study has highlighted the synchrony of different phases of formation of the PG and major regional climate variability, suggesting that formation of the influenced regional climate, particularly the prevailing local winds. How did the its formation affect the Shamal wind? What are the implications of its formation for understanding dust emission variability during the Holocene? Future studies should address these questions.

Acknowledgements. The authors thank M. Pourkerman, P. Habibi and M. Hosseindoost from INIOAS for their help in sampling and sedimentological analyses, and T. Tuna and Y. Fagault from CEREGE for help with ^{14}C analyses. The authors sincerely thank the anonymous reviewers for their time and constructive feedback, which enhanced the scientific quality and presentation of the manuscript. This work was supported by: The Iranian National Institute for Oceanography and Atmospheric Science (INIOAS) in the framework of the project No. INIOAS-1400-012-01-08-03; Center for International Scientific Studies and Collaborations (CISSC), Ministry of Science, Research and Technology of Iran; Campus France in the framework of a project entitled: paleo-temperature and paleo-productivity of the Persian Gulf during the Holocene based on stable isotope geochemistry; and Labex OT-MED (OSU PYTHEAS, CNRS, Aix-Marseille Université) through the project 'Paradise Lost'.

Data availability statement

I agree to share my data along with my accepted paper.

Supporting information

Additional supporting information may be found in the online version of this article at the publisher's web-site.

Figure S1. Correlation of core PG-51 and its sister core, PG-51S based on magnetic susceptibility log. Black circles (PG-51) represent the dated samples in uncalibrated BP and red circles are corresponding horizons in core PG-51S based on correlated magnetic susceptibility logs. The correlated horizons are indicated by gray bands. The blue circles indicate a dated horizon based on reconstructed Clam age-depth model in core PG-51 and its equivalent depth in core PG-51S.

Figure S2. Pollen diagram of the PG-51 core. All plant pollen taxa (and Sporormiella) are represented as pollen percentages over the Total Pollen Sum including aquatic pollen (Sparganium-type+Cyperaceae+Riella). Please note that most of the pollen spectra are from the early Holocene.

Figure S3. Comparison of the zonation schemes of the core PG-51/51S and PG-104 based on different proxies which are mentioned in the text. The colored areas indicate the critical periods of environmental changes that are reflected by higher frequency of the shifts in the zones of different proxies.

Abbreviations. ASH, Arabian Shallow Shelf; CEREGE, Centre de recherche et d'enseignement des géosciences de l'environnement; CISSC, Center for International Scientific Studies and Collaborations; CNRS, Centre national de la recherche scientifique; ESB, Eastern Sub-Basin; GC, gas chromatography; INIOAS, Iranian National Institute for Oceanography and Atmospheric Science; IMBE, Institut Méditerranéen de Biodiversité et d'Ecologie; IOSM, Indian Ocean Summer Monsoon; ITCZ, Inter-Tropical Convergence Zone; MLW, mid-latitude Westerlies; MSS, Mesopotamian Shallow Shelf; MS, magnetic susceptibility; MRA, marine reservoir age; PG, Persian Gulf; PCA, principal component analysis; TOM, total organic matter; TOC, total organic carbon; TN, total nitrogen; TC, total carbon; WSB, Western Sub-Basin; XRF, X-ray fluorescence.

References

Akhani, H. (2006) Biodiversity of halophytic and sabkha ecosystems in Iran. In: Khan, M.A., Böer, B., Kust, G.S. & Barth, H.J. (Eds.) *Sabkha Ecosystems. Volume II: West and Central Asia*. Springer. pp. 71–88.

Al-Yamani, F. 2008. Importance of the freshwater influx from the Shatt-Al-Arab River on the Gulf marine environment. Protecting the Gulf's marine ecosystems from pollution. Springer. pp. 207–222.

Bard, E., Tuna, T., Fagault, Y., Bonvalot, L., Wacker, L., Fahrni, S. et al. (2015) AixMICADAS, the accelerator mass spectrometer dedicated to 14C recently installed in Aix-En-Provence, France. *Nuclear Instruments and Methods in Physics Research Section B: Beam Interactions with Materials and Atoms*, 361, 80–86. Available at: https://doi.org/10.1016/j.nimb.2015.01.075

Bar-Matthews, M. & Ayalon, A. (2011) Mid-Holocene climate variations revealed by high-resolution speleothem records from Soreq Cave, Israel and their correlation with cultural changes. *The Holocene*, 21(1), 163–171.

Behbahani, R., Hosseinyar, G. & Lak, R. (2015) The controlling parameters on organic matter preservation within the bottom sediments of the northern part of the Persian Gulf. *Neues Jahrbuch für Geologie und Paläontologie - Abhandlungen*, 276(3), 267–283.

Bond, G., Showers, W., Cheseby, M., Lotti, R., Almasi, P., DeMenocal, P. et al. (1997) A pervasive millennial-scale cycle in North Atlantic Holocene and glacial climates. *Science*, 278(5341), 1257–1266.

Bottema, S. & Woldring, H. (1990) Anthropogenic indicators in the pollen diagrams of the Eastern Mediterranean. In: Bottema, S., Entjes-NieBbio, G. & van Zeist, W. (Eds.) *Man's role in the shaping of the Eastern Mediterranean landscape*. Rotterdam: Balkema. pp. 231–264.

Bradley, R.S. (2000) Past global changes and their significance for the future. *Quaternary Science Reviews*, 19(1–5), 391–402.

Brassell, S.C., Eglinton, G., Marlowe, I.T., Pflaumann, U. & Sarnthein, M. (1986) Molecular stratigraphy: A new tool for climatic assessment. *Nature*, 320, 129–133.

Bray, E.E. & Evans, E.D. (1961) Distribution of n-paraffins as a clue to recognition of source beds. *Geochimica et Cosmochimica Acta*, 22, 2–15.

Büntgen, U., Myglan, V.S., Ljungqvist, F.C., McCormick, M., Di Cosmo, N., Sigl, M. et al. (2016) Cooling and societal change during the Late Antique Little Ice Age from 536 to around 660 AD. *Nature Geoscience*, 9(3), 231–236.

Bush, R.T. & McInerney, F.A. (2015) Influence of temperature and C$_4$ abundance on *n*-alkane chain length distributions across the central USA. *Organic Geochemistry*, 79, 65–73.

Calvert, S.E. & Pedersen, T.F. (1992) Organic carbon accumulation and preservation in marine sediments: how important is anoxia. In: Whelan, J.K. & Farrington, J.W. (Eds.) *Organic Matter, productivity, accumulation and preservation of organic matter in recent and ancient sediments*. New York: Columbia University Press. pp. 231–263.

Castañeda, I.S. & Schouten, S. (2011) A review of molecular organic proxies for examining modern and ancient lacustrine environments. *Quaternary Science Reviews*, 30(21–22), 2851–2891.

Conte, M.H., Volkman, J.K. & Eglinton, G. 1994. Lipid bio-markers of the Haptophyta. In: Green, J.C., Leadbeater, B.S.C. (Eds.) *The Haptophyte Algae*. Systematics Association, Special Volume 51, pp. 351–377.

D'Andrea, W.J., Lage, M., Martiny, J.B.H., Laatsch, A.D., Amaral-Zettler, L.A., Sogin, M.L. et al. (2006) Alkenone producers inferred from well-preserved 18S rDNA in Greenland lake sediments. *Journal of Geophysical Research: Biogeosciences*, 111, G03013. Available at: https://doi.org/10.1029/2005JG000121

D'Andrea, W.J., Vaillencourt, D.A., Balascio, N.L., Werner, A., Roof, S.R., Retelle, M. et al. (2012) Mild Little Ice Age and unprecedented recent warmth in an 1800 year lake sediment record from Svalbard. *Geology*, 40, 1007–1010. Available at: https://doi.org/10.1130/G33365.1

Djamali, M., Akhani, H., Andrieu-Ponel, V., Braconnot, P., Brewer, S., de Beaulieu, J.-L. et al. (2010) Indian Summer Monsoon variations could have affected the early-Holocene woodland expansion in the Near East. *The Holocene*, 20(5), 813–820.

Djamali, M., Akhani, H., Khoshravesh, R., Andrieu-Ponel, V., Ponel, P. & Brewer, S. (2011) Application of the global bioclimatic classification to Iran: implications for understanding the modern vegetation and biogeography. *Ecologia mediterranea*, 37(1), 91–114.

Djamali, M., de Beaulieu, J.-L., Miller, N.F., Andrieu-Ponel, V., Ponel, P., Lak, R. et al. (2009) Vegetation history of the SE section of the Zagros Mountains during the last five millennia; a pollen record from the Maharlou Lake, Fars Province, Iran. *Vegetation History and Archaeobotany*, 18, 123–136.

Djamali, M., de Beaulieu, J.-L., Shah-hosseini, M., Andrieu-Ponel, V., Ponel, P., Amini, A. et al. (2008) A late Pleistocene long pollen record from Lake Urmia, NW Iran. *Quaternary Research*, 69(3), 413–420.

Djamali, M., Brewer, S., Breckle, S.W. & Jackson, S.T. (2012) Climatic determinism in phytogeographic regionalization: a test from the Irano-Turanian region, SW and Central Asia. *Flora-Morphology, Distribution, Functional Ecology of Plants*, 207(4), 237–249.

Dolman, A.M., Groeneveld, J., Mollenhauer, G., Ho, S.L. & Laepple, T. (2021) Estimating bioturbation from replicated small-sample radiocarbon ages. *Paleoceanography and Paleoclimatology*, 36, e2020PA004142.

Eglinton, G. & Hamilton, R.J. (1967) Leaf Epicuticular Waxes: The waxy outer surfaces of most plants display a wide diversity of fine structure and chemical constituents. *Science*, 156(3780), 1322–1335.

Faegri, K. & Iversen, J. 1975. Text book of pollen analysis. Hafner, New York, New York, USA.

Fagault, Y., Tuna, T., Rostek, F. & Bard, E. (2019) Radiocarbon dating small carbonate samples with the gas ion source of AixMICADAS. *Nuclear Instruments and Methods in Physics Research Section B: Beam Interactions with Materials and Atoms*, 455, 276–283.

Fleitmann, D., Burns, S.J., Mangini, A., Mudelsee, M., Kramers, J., Villa, I. et al. (2007) Holocene ITCZ and Indian monsoon dynamics recorded in stalagmites from Oman and Yemen (Socotra). *Quaternary Science Reviews*, 26(1), 170–188.

Fleitmann, D., Burns, S.J., Mudelsee, M., Neff, U., Kramers, J., Mangini, A. et al. (2003) Holocene forcing of the Indian monsoon recorded in a stalagmite from southern Oman. *Science*, 300(5626), 1737–1739.

Gupta, A.K., Anderson, D.M. & Overpeck, J.T. (2003) Abrupt changes in the Asian southwest monsoon during the Holocene and their links to the North Atlantic Ocean. *Nature*, 421(6921), 354–357.

Hamzeh, M.A., Khosravi, M., Carton, X., Yarahmadi, D. & Safarkhani, E. (2021) Paleoceanography of the Strait of Hormoz and its link to paleoclimate changes since the mid-Holocene. *Continental Shelf Research*, 226, 104507.

Hari, V., Villarini, G., Karmakar, S., Wilcox, L.J. & Collins, M. (2020) Northward propagation of the intertropical convergence zone and strengthening of Indian summer monsoon rainfall. *Geophysical Research Letters*, 47(23), e2020GL089823.

Heaton, T.J., Blaauw, M., Blackwell, P.G., Bronk Ramsey, C., Reimer, P.J. & Scott, E.M. (2020) The IntCal20 Approach to Radiocarbon Calibration Curve Construction: A New Methodology Using Bayesian Splines and Errors-in-Variables. *Radiocarbon*, 62(4), 821–863. Available at: https://doi.org/10.1017/RDC.2020.68

Heidarzadeh, M., Šepić, J., Rabinovich, A., Allahyar, M., Soltanpour, A. & Tavakoli, F. (2020) Meteorological tsunami of 19 March 2017 in the Persian Gulf: observations and analyses. *Pure and Applied Geophysics*, 177(3), 1231–1259.

Heyvaert, V.M.A. & Baeteman, C. (2007) Holocene sedimentary evolution and palaeocoastlines of the Lower Khuzestan plain (southwest Iran). *Marine Geology*, 242(1–3), 83–108.

Horikawa, K., Murayama, M., Minagawa, M., Kato, Y. & Sagawa, T. (2010) Latitudinal and downcore (0–750 ka) changes in *n*-alkane chain lengths in the eastern equatorial Pacific. *Quaternary Research*, 73, 573–582.

Hosseinyar, G., Behbahani, R., Moussavi-Harami, R., Lak, R. & Kuijpers, A., 2021. Holocene sea-level changes of the Persian Gulf: Quaternary International. 571, 26-45.

Isaev, V.A. & Mikhailova, M.V. (2009) The hydrography, evolution, and hydrological regime of the mouth area of the Shatt al-Arab River. *Water resources*, 36, 380–395.

Kämpf, J. & Sadrinasab, M. (2006) The circulation of the Persian Gulf: a numerical study. *Ocean Science*, 2(1), 27–41.

Kaniewski, D., Marriner, N., Cheddadi, R., Guiot, J. & Van Campo, E. (2018) The 4.2 ka BP event in the Levant. *Climate of the Past*, 14(10), 1529–1542.

Kennett, D.J. & Kennett, J.P. (2007) Influence of Holocene marine transgression and climate change on cultural evolution in southern Mesopotamia, *Climate Change and Cultural Dynamics*. Elsevier. pp. 229–264

Konyuhov, A.I. & Maleki, B. (2006) The Persian Gulf Basin: Geological history, sedimentary formations, and petroleum potential. *Lithology and Mineral Resources*, 41(4), 344–361.

Lambeck, K. (1996) Shoreline reconstructions for the Persian Gulf since the last glacial maximum. *Earth and Planetary Science Letters*, 142(1–2), 43–57.

Leider, A., Hinrichs, K.-U., Schefuß, E. & Versteegh, G.J.M. (2013) Distribution and stable isotopes of plant wax derived *n*-alkanes in lacustrine, fluvial and marine surface sediments along an Eastern Italian transect and their potential to reconstruct the hydrological cycle. *Geochimica et Cosmochimica Acta*, 117, 16–32.

Leuschner, D.C., Sirocko, F., Grootes, P.M. & Erlenkeuser, H. (2002) Possible influence of Zoophycos bioturbation on radiocarbon dating and environmental interpretation. *Marine Micropaleontology*, 46(1–2), 111–126.

Liu, J.P. & Milliman, J.D. (2004) Reconsidering melt-water pulses 1A and 1B: global impacts of rapid sea-level rise. *Journal of Ocean University of China*, 3(2), 183–190.

Meyers, P.A. 2003) Applications of organic geochemistry to paleolimnological reconstructions: a summary of examples from the Laurentian Great Lakes. *Organic Geochemistry*, 34(2), 261–289.

Meyers, P.A. & Ishiwatari, R. (1993) Lacustrine organic geochemistry—an overview of indicators of organic matter sources and diagenesis in lake sediments. *Organic Geochemistry*, 20(7), 867–900.

Mix, A. (2001) Environmental processes of the ice age: land, oceans, glaciers (EPILOG). *Quaternary Science Reviews*, 20(4), 627–657.

Naderi Beni, A., Marriner, N., Sharifi, A., Azizpour, J., Kabiri, K., Djamali, M. et al. (2021) Climate change: A driver of future conflicts in the Persian Gulf Region. *Heliyon*, 7(2), e06288. Available at: https://doi.org/10.1016/j.heliyon.2021.e06288

Nagashima, K., Tada, R. & Matsui, H. (2004) Intensity variation in the Asian monsoon and the Westerly during the last 140kyr deduced from grain size analysis of Japan Sea sediments. *The Quaternary Research (Daiyonki-Kenkyu)*, 43(2), 85–97.

Nowroozi, A.A. & Ahmadi, G. (1986) Analysis of earthquake risk in Iran based on seismotectonic provinces. *Tectonophysics*, 122(1–2), 89–114.

Pakhomova, S.V., Hall, P.O.J., Kononets, M.Y., Rozanov, A.G., Tengberg, A. & Vershinin, A.V. (2007) Fluxes of iron and manganese across the sediment–water interface under various redox conditions. *Marine Chemistry*, 107(3), 319–331.

Palchan, D. & Torfstein, A. (2019) A drop in Sahara dust fluxes records the northern limits of the African Humid Period. *Nature Communications*, 10(1), 3803. Available at: https://doi.org/10.1038/s41467-019-11701-z

Parker, A.G., Eckersley, L., Smith, M.M., Goudie, A.S., Stokes, S., Ward, S. et al. (2004) Holocene vegetation dynamics in the northeastern Rub'al Khali desert, Arabian Peninsula: a phytolith, pollen and carbon isotope study. *Journal of Quaternary Science*, 19(7), 665–676.

Parker, A.G., Goudie, A.S., Stokes, S., White, K., Hodson, M.J., Manning, M. et al. (2006) A record of Holocene climate change from lake geochemical analyses in southeastern Arabia. *Quaternary Research*, 66(3), 465–476.

Parker, J.G. (1983) A comparison of methods used for the measurement of organic matter in marine sediment. *Chemistry and Ecology*, 1(3), 201–209.

Perdue, E.M. & Koprivnjak, J.F. (2007) Using the C/N ratio to estimate terrigenous inputs of organic matter to aquatic environments. *Estuarine, Coastal and Shelf Science*, 73(1-2), 65–72.

Pous, S., Carton, X. & Lazure, P. (2012) A process study of the tidal circulation in the Persian Gulf. *Open Journal of Marine Science*, 02(4), 131–140.

Pous, S., Carton, X. & Lazure, P. (2013) A process study of the wind-induced circulation in the Persian Gulf. *Open Journal of Marine Science*, 03(1), 1–11.

Pous, S., Lazure, P. & Carton, X. (2015) A model of the general circulation in the Persian Gulf and in the Strait of Hormuz: Intraseasonal to interannual variability. *Continental Shelf Research*, 94, 55–70.

Prahl, F.G., De Lange, G.J., Lyle, M. & Sparrow, M.A. (1989) Post-depositional stability of long-chain alkenones under contrasting redox conditions. *Nature*, 341(6241), 434–437.

Purser, B.H. (2012) *The Persian Gulf: Holocene carbonate sedimentation and diagenesis in a shallow epicontinental sea*. Springer Science & Business Media.

Pye, K. (1987) *Aeolian dust and dust deposits*. London: Academic Press. p. 334.

Reimer, P.J. & Reimer, R.W. (2001) A marine reservoir correction database and on-line interface. *Radiocarbon*, 43, 461–463.

Richter, T.O., Van der Gaast, S., Koster, B., Vaars, A., Gieles, R., de Stigter, H.C. et al. (2006) The Avaatech XRF Core Scanner: technical description and applications to NE Atlantic sediments. *Geological Society, London, Special Publications*, 267(1), 39–50.

Rommerskirchen, F., Plader, A., Eglinton, G., Chikaraishi, Y. & Rullkötter, J. (2006) Chemotaxonomic significance of distribution and stable carbon isotopic composition of long-chain alkanes and alkan-1-ols in C4 grass waxes. *Organic Geochemistry*, 37, 1303–1332.

Safaierad, R., Mohtadi, M., Zolitschka, B., Yokoyama, Y., Vogt, C. & Schefuß, E. 2020. Elevated dust depositions in West Asia linked to ocean–atmosphere shifts during North Atlantic cold events. Proceedings of the National Academy of Sciences. 117 (31), 18272–18277.

Saleh, A., Abtahi, B., Mirzaei, N., Chen, C.T.A., Ershadifar, H., Ghaemi, M. et al. (2021) Hypoxia in the Persian Gulf and the Strait of Hormuz. *Marine Pollution Bulletin*, 167, 112354.

Schwab, V.F. & Sachs, J.P. (2011) Hydrogen isotopes in individual alkenones from the Chesapeake Bay estuary. *Geochimica et Cosmochimica Acta*, 75(23), 7552–7565.

Seki, O., Okazaki, Y. & Harada, N. (2021) Assessment of long-chain *n*-alkanes as a paleoclimate proxy in the Bering Sea sediments. *Progress in Oceanography*, 198, 102687.

Sharifi, A., Murphy, L.N., Pourmand, A., Clement, A.C., Canuel, E.A., Naderi Beni, A. et al. (2018) Early-Holocene greening of the Afro-Asian dust belt changed sources of mineral dust in West Asia. *Earth and Planetary Science Letters*, 481, 30–40.

Sharifi, A., Pourmand, A., Canuel, E.A., Ferer-Tyler, E., Peterson, L.C., Aichner, B. et al. (2015) Abrupt climate variability since the last deglaciation based on a high-resolution, multi-proxy peat record from NW Iran: The hand that rocked the Cradle of Civilization? *Quaternary Science Reviews*, 123, 215–230.

Sholkovitz, E.R. (1978) The flocculation of dissolved Fe, Mn, Al, Cu, NI, Co and Cd during estuarine mixing. *Earth and Planetary Science Letters*, 41(1), 77–86.

Sicre, M.A., Gagosian, R.B. & Peltzer, E.T. (1990) Evaluation of the atmospheric transport of marine-derived particles using long-chain unsaturated ketones. *Journal of Geophysical Research: Atmospheres*, 95(D2), 1789–1795.

Sirocko, F., Sarnthein, M., Erlenkeuser, H., Lange, H., Arnold, M. & Duplessy, J.C. (1993) Century-scale events in monsoonal climate over the past 24,000 years. *Nature*, 364(6435), 322–324.

Smith, D.E., Harrison, S., Firth, C.R. & Jordan, J.T. (2011) The Early-Holocene sea level rise. *Quaternary Science Reviews*, 30(15–16), 1846–1860.

Southon, J., Kashgarian, M., Fontugne, M., Metivier, B. & W-S yim, W. (2002) Marine reservoir corrections for the Indian Ocean and Southeast Asia. *Radiocarbon*, 44(1), 167–180.

Stevens, L.R., Wright Jr., H.E. & Ito, E. (2001) Proposed changes in seasonality of climate during the Lateglacial and Holocene at Lake Zeribar, Iran. *The Holocene*, 11(6), 747–755.

Taylor, A.K., Benedetti, M.M., Haws, J.A. & Lane, C.S. (2018) Mid-Holocene Iberian hydroclimate variability and paleoenvironmental change: molecular and isotopic insights from Praia Rei Cortiço, Portugal. *Journal of Quaternary Science*, 33(1), 79–92.

Thiel, V., Jenisch, A., Landmann, G., Reimer, A. & Michaelis, W. (1997) Unusual distributions of long-chain alkenones and tetrahymanol from the highly alkaline Lake Van, Turkey. *Geochimica et Cosmochimica Acta*, 61(10), 2053–2064.

Thoppil, P.G. & Hogan, P.J. (2010) Persian Gulf response to a wintertime shamal wind event. *Deep Sea Research Part I: Oceanographic Research Papers*, 57(8), 946–955.

Tjallingii, R., Röhl, U., Kölling, M. & Bickert, T. (2007) Influence of the water content on X-ray fluorescence core-scanning measurements in soft marine sediments. *Geochemistry, Geophysics, Geosystems*, 8(2), Q02004.

Tuna, T., Fagault, Y., Bonvalot, L., Capano, M. & Bard, E. (2018) Development of small CO2 gas measurements with AixMICADAS. *Nuclear Instruments and Methods in Physics Research Section B: Beam Interactions with Materials and Atoms*, 437, 93–97.

Uchupi, E., Swift, S.A. & Ross, D.A. (1999) Late Quaternary stratigraphy, paleoclimate and neotectonism of the Persian (Arabian) Gulf region. *Marine Geology*, 160(1), 1–23.

Verardo, D.J., Froelich, P.N. & McIntyre, A. (1990) Determination of organic carbon and nitrogen in marine sediments using the Carlo Erba NA-1500 analyzer. *Deep Sea Research Part A. Oceanographic Research Papers*, 37(1), 157–165.

Vogts, A., Schefuß, E., Badewien, T. & Rullkötter, J. (2012) *n*-Alkane parameters from a deep sea sediment transect off southwest Africa reflect continental vegetation and climate conditions. *Organic Geochemistry*, 47, 109–119.

Volkman, J.K., Barrerr, S.M., Blackburn, S.I. & Sikes, E.L. (1995) Alkenones in Gephyrocapsa oceanica: Implications for studies of paleoclimate. *Geochimica et Cosmochimica Acta*, 59(3), 513–520.

Weltje, G., Bloemsma, M., Tjallingii, R., Heslop, D., Röhl, U. & Croudace, I.W., 2015. Prediction of Geochemical Composition from XRF Core Scanner Data: A New Multivariate Approach Including Automatic Selection of Calibration Samples and Quantification of Uncertainties. Micro-XRF Studies of Sediment Cores, Springer, 507-534.

Weltje, G.J. & Tjallingii, R. (2008) Calibration of XRF core scanners for quantitative geochemical logging of sediment cores: Theory and application. *Earth and Planetary Science Letters*, 274(3–4), 423–438.

Xu, B., Burnett, W., Dimova, N., Diao, S., Mi, T., Jiang, X. et al. (2013) Hydrodynamics in the Yellow River Estuary via radium isotopes: Ecological perspectives. *Continental Shelf Research*, 66, 19–28.

Ziegler, M., Jilbert, T., de Lange, G.J., Lourens, L.J. & Reichart, G.J. (2008) Bromine counts from XRF scanning as an estimate of the marine organic carbon content of sediment cores. *Geochemistry, Geophysics, Geosystems*, 9(5), Q05009. Available at: https://doi.org/10.1029/2007GC001932